JOURNAL OF COMPUTATIONAL PHYSICS 121, 155–175 (1995)

Direct Numerical Simulation of Flow in a Channel with Complex, Time-Dependent Wall Geometries: A Pseudospectral Method

H. A. CARLSON,*[,1] G. BERKOOZ,† AND J. L. LUMLEY*

*Department of Mechanical and Aerospace Engineering, Cornell University, Ithaca, New York 14850; and †BEAM Technologies Inc., Ithaca, New York 14850

Received June 7, 1994; revised January 6, 1995

An algorithm has been developed which extends the scope of spectral methods to include solution of non-canonical channel flows arising from more complicated wall geometries. This significantly broadens the direct numerical simulation data base and its range of application, providing an accurate tool for the investigation of flows over three-dimensional surfaces which move in time. Through a time-dependent, curvilinear transformation a general domain is mapped to one which permits spectral representation of the solution and preserves exact boundary conditions. Beginning with the Navier–Stokes equation in general tensor form, application of a metric operator effects the transformation. The primitive variables are represented pseudospectrally (Fourier in the stream- and spanwise directions, Chebyshev wall-normal). Covariant differentiation generates variable coefficient terms in the equations for pressure and velocity, necessitating an iterative solution scheme. Standard benchmark tests validate flat-wall flow simulations. Static and dynamic tests of one-dimensional flow over a perturbed wall confirm the accuracy of the time-dependent transformation. Low Reynolds number simulations replicate the appropriate qualitative features of Stokes flow across two- and three-dimensional wall topographies. Results from a higher Reynolds number simulation of separated flow behind a three-dimensional Gaussian protuberance match well with an independent solution from Mason and Morton who have used a finite-difference method.

1. INTRODUCTION

Owing to its accuracy and efficiency and the suitability of its solution form (for analysis), a pseudospectral (PS) approach has become the method of choice for many problems in computational fluid dynamics. Three-dimensional flow between two flat boundaries (channel flow) has been studied extensively using the spectral technique and the results have contributed to the understanding of transitional flows [1–3] and turbulent boundary layer dynamics [4–6]. But given the range of complexity of problems in the field, particularly those borne by industry, there remains a shortfall in the scope and flexibility that available computational tools provide.

Generalizing the three-dimensional channel flow problem by specifying more than the simplest domain has heretofore forced either an abandonment of the spectral method for less accurate, often prohibitively expensive finite-difference techniques [7, 8] or an adjustment from direct numerical simulation (DNS) to modeling [9, 10]. Domain decomposition and available hybrid methods such as the spectral-element approach [11] place substantial restrictions on the allowable topographies. This article describes a pseudospectral method which, coupled with a curvilinear coordinate transformation, permits direct solution of the Navier–Stokes equation in a three-dimensional domain delimited by non-trivial, time-dependent boundaries.

Motivation for the work comes out of an ongoing investigation of near-wall turbulence aimed at effecting drag reduction by controlling the wall-layer dynamics [12–14]. The algorithm was developed to serve as a tool in this effort (smart skin simulation): an actuator on the wall responds to a flow through sensors and a feedback control loop, adjusting its height in order to steer the wall region dynamics (the bursting processes which are signatures of turbulent flows and primary sources of drag). More generally the method extends the range of application of direct simulation with spectral decomposition to a hitherto inaccessible class of problems.

Designating a domain with flat, stationary boundaries as the canonical channel, wall perturbations in the non-canonical channel may range from 0 to 10% of the total channel height, the maximum depending upon the wall topography. All simulations begin with parabolic flow between two flat walls. The top wall remains flat; the bottom wall perturbation is $h(\tilde{x}_1, \tilde{x}_3, t)$. In Euclidian space the streamwise, wall-normal, and spanwise directions are denoted as $\tilde{x}_1, \tilde{x}_2$, and $\tilde{x}_3$, respectively. Wall geometries are restricted to Fourier-transformable functions.

The equation to be solved (non-dimensionalized and in rotational form) is

$$\frac{\partial \mathbf{u}}{\partial t} = -\nabla p + \mathbf{u} \times (\nabla \times \mathbf{u}) + \frac{1}{\mathrm{Re}} \nabla^2 \mathbf{u} \tag{1.1}$$

$$p \equiv \tilde{p} + \frac{1}{2} \mathbf{u} \cdot \mathbf{u}. \tag{1.2}$$

[1] E-mail: hal@mae.cornell.edu.

0021-9991/95 $12.00

The Reynolds number (Re) is based on mean streamwise velocity at mid-channel (U_0) and on the channel half-height (L_0):

$$\mathrm{Re} = \frac{U_0 L_0}{\nu}. \tag{1.3}$$

Units of velocity, length, and time are normalized then by U_0, L_0, and L_0/U_0, respectively. The velocity $\mathbf{u}$ and modified pressure p may be represented spectrally (Fourier in $\tilde{x}_1$ and $\tilde{x}_3$, Chebyshev in $\tilde{x}_2$). The solution is therefore periodic in $\tilde{x}_1$ and $\tilde{x}_3$. The domain consists of solid boundaries at $\tilde{x}_2 = \pm 1$ (in the case of the simple channel), requiring no-slip, no-penetration boundary conditions on velocity. The velocity vector is

$$\mathbf{u}(\tilde{x}_1, \tilde{x}_2, \tilde{x}_3, t) = \sum_{k_3=-\infty}^{+\infty} \sum_{k_2=0}^{+\infty} \sum_{k_1=0}^{+\infty} \mathbf{a}(k_1, k_2, k_3, t) S_{k_2}(\tilde{x}_2) e^{2\pi i k_1 \tilde{x}_1 / L_1} e^{2\pi i k_3 \tilde{x}_3 / L_3} + \text{c.c.} \tag{1.4}$$

$$S_{k_2}(\tilde{x}_2) \equiv \cos[k_2 \cos^{-1}(\tilde{x}_2)]. \tag{1.5}$$

Because $\mathbf{u}$ is a real-valued function, c.c. in (1.4) is the complex conjugate. Unless otherwise specified "mean" is defined as the value of the coefficient $\mathbf{a}$ corresponding to the zeroth Fourier mode combination ($k_{1,3} = 0$). Viscosity is constant and flow is solenoidal (incompressible):

$$\nabla \cdot \mathbf{u} = 0. \tag{1.6}$$

Modified pressure is defined as a scalar function which, when substituted into (1.1), satisfies (1.6) everywhere in the domain

$$\nabla^2 p = \nabla \cdot [\mathbf{u} \times (\nabla \times \mathbf{u})]. \tag{1.7}$$

Flow is sustained (viscous effects are overcome) through the inclusion of a mean streamwise pressure gradient: either a specified constant or a variable value which maintains a constant mass flux. In the case of steady, parabolic flow between two flat walls, the gradient ($\partial p/\partial x_1 = -2/\mathrm{Re}$) yields a constant mass flux in the streamwise direction and this is the value specified when using the constant gradient option. A time-dependent gradient which maintains constant mass flux for any flow is derived by integrating the Navier–Stokes equation over the Euclidian domain and enforcing the following condition:

$$\int_0^{L_3} \int_{h-1}^{+1} \int_0^{L_1} \frac{\partial \tilde{u}^1}{\partial t} \, d\tilde{x}_1 \, d\tilde{x}_2 \, d\tilde{x}_3 = 0. \tag{1.8}$$

2. THE ALGORITHM

This section contains a description of the algorithm including the coordinate transformation, the discretization and the iterative method, the prescription of the boundary conditions, the influence matrix formulation, the tau correction, and the time integration method.

2.1. *The Coordinate Transformation*

The equations of motion are solved by first transforming from Euclidian space to a generalized coordinate frame [15–17]. More than a mapping of the domain, the transformation reconstructs the solution vectors, so that *all* boundary conditions remain exact. The physical frame is represented in Cartesian coordinates ($\tilde{x}_i$) and the computational frame in general curvilinear coordinates (x_i). The transformation is defined by the following relations:

$$\begin{aligned} \tilde{x}_1 &= x_1 \\ \tilde{x}_2 &= T(x_1, x_2, x_3, x_4) \\ T &\equiv \frac{(2-h)x_2 + h}{2} \\ \tilde{x}_3 &= x_3 \\ \tilde{x}_4 &= x_4 \quad \text{(time)}. \end{aligned} \tag{2.1}$$

The transformation tensor is

$$c_j^i = \frac{\partial \tilde{x}_i}{\partial x_j}, \tag{2.2}$$

and in matrix form,

$$\mathbf{C} = \begin{pmatrix} 1 & 0 & 0 & 0 \\ \dfrac{\partial T}{\partial x_1} & \dfrac{\partial T}{\partial x_2} & \dfrac{\partial T}{\partial x_3} & \dfrac{\partial T}{\partial x_4} \\ 0 & 0 & 1 & 0 \\ 0 & 0 & 0 & 1 \end{pmatrix}. \tag{2.3}$$

Because spatial and temporal derivatives in the Navier–Stokes equation are distinct, the time derivative term may be treated separately and a three-dimensional metric based on the space variables defined:

$$g_{ij} = \sum_{k=1}^{3} c_i^k c_j^k. \tag{2.4}$$

The transformation is non-orthogonal: diagonal entries of the metric are of order one, off-diagonal are of order h or h^2. The corresponding symmetric matrix is

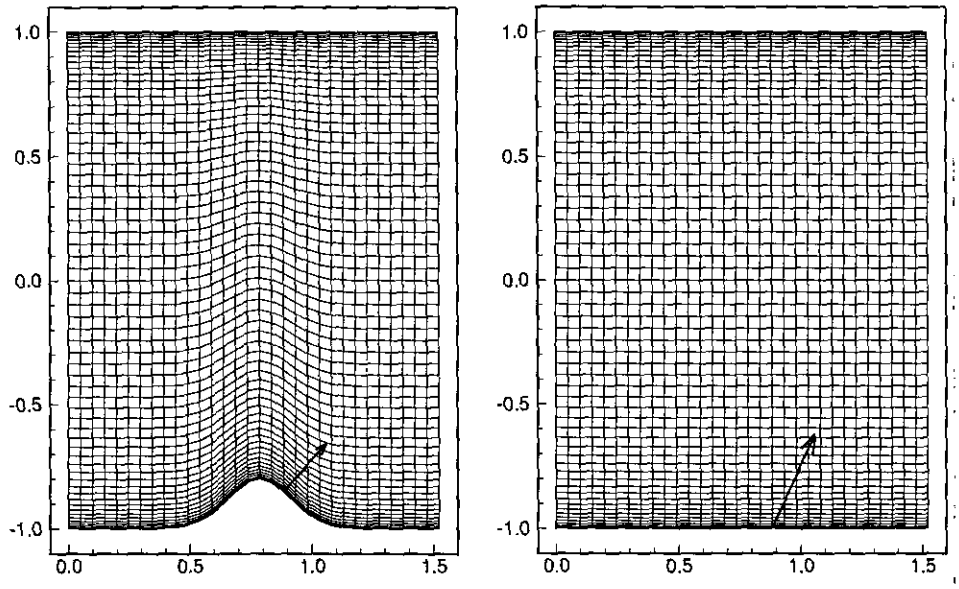

FIG. 1. Front views of the physical coordinate frame (left) and the computational frame (right) showing the transformation of a representative vector, normal to the lower wall. The transformation is non-orthogonal.

$$\mathbf{G} = \begin{pmatrix} 1 + \left(\frac{\partial T}{\partial x_1}\right)^2 & \frac{\partial T}{\partial x_1}\frac{\partial T}{\partial x_2} & \frac{\partial T}{\partial x_1}\frac{\partial T}{\partial x_3} \\ \frac{\partial T}{\partial x_2}\frac{\partial T}{\partial x_1} & \left(\frac{\partial T}{\partial x_2}\right)^2 & \frac{\partial T}{\partial x_2}\frac{\partial T}{\partial x_3} \\ \frac{\partial T}{\partial x_3}\frac{\partial T}{\partial x_1} & \frac{\partial T}{\partial x_3}\frac{\partial T}{\partial x_2} & 1 + \left(\frac{\partial T}{\partial x_3}\right)^2 \end{pmatrix}. \tag{2.5}$$

The Jacobian is

$$J \equiv |\mathbf{G}|^{1/2} \equiv |\mathbf{C}| = \frac{\partial T}{\partial x_2}; \tag{2.6}$$

$|\ |$ denotes the determinant. Contravariant components of the velocity vector transform as follows:

$$\tilde{u}^j = c_i^j u^i \quad (i, j = 1, 3). \tag{2.7}$$

From the definition of the transformation tensor (2.2), a change in orientation is ascribed only to the wall-normal component of velocity (Fig. 1):

$$\begin{aligned} \tilde{u}^1 &= u^1 \\ \tilde{u}^2 &= \frac{\partial T}{\partial x_1} u^1 + \frac{\partial T}{\partial x_2} u^2 + \frac{\partial T}{\partial x_3} u^3 \\ \tilde{u}^3 &= u^3 \end{aligned} \tag{2.8}$$

In general tensor form the Navier–Stokes equation is

$$\frac{\partial u^i}{\partial \tilde{t}} + u^j u^i_{,j} = -(g^{ij}\tilde{p})_{,j} + \frac{1}{\mathrm{Re}}(u_{i,j} + u_{j,i})_{,j}. \tag{2.9}$$

A comma with index denotes covariant differentiation (in the computational frame):

$$u^i_{,j} = \frac{\partial u^i}{\partial x_j} + \Gamma^i_{jk} u^k \tag{2.10}$$

$$\Gamma^i_{jk} \equiv \frac{1}{2} g^{il}\left[\frac{\partial}{\partial x_j}(g_{kl}) + \frac{\partial}{\partial x_k}(g_{jl}) - \frac{\partial}{\partial x_l}(g_{jk})\right]; \tag{2.11}$$

$\tilde{t}$ in (2.9) denotes time in the Euclidian frame. In the computational frame, the time derivative becomes

$$\frac{\partial u^i}{\partial \tilde{t}} = \frac{\partial u^i}{\partial t} + \frac{\partial T}{\partial t}\frac{\partial u^i}{\partial x_2}. \tag{2.12}$$

The following identity is used to convert the equation to rotational form:

$$u^j u^i_{,j} = u^j g^{ik}(u_{k,j} - u_{j,k}) + \tfrac{1}{2} g^{ik}(u^j u_j)_{,k}. \tag{2.13}$$

The last term in (2.13) is absorbed by the pressure gradient. With solenoidal flow, conservation of mass yields

$$u^i_{,i} = \frac{\partial}{\partial x_i}(J u^i) = 0. \tag{2.14}$$

The solenoidal condition eliminates the second half of the vis-

cous term in (2.9) and the final (continuous) form of the evolution equation for velocity is

$$\frac{\partial u^i}{\partial t} = -\frac{\partial T}{\partial t}\frac{\partial u^i}{\partial x_2} + u^j g^{ik}(u_{j,k} - u_{k,j}) - g^{ij}\frac{\partial p}{\partial x_j} + \frac{1}{\mathrm{Re}}(g^{jk}u^i_{,k})_{,j}. \tag{2.15}$$

Utilizing the fact that the metric commutes with the divergence (covariant derivative) operator, (2.14) and (2.15) yield a relation for pressure:

$$\left(g^{ij}\frac{\partial p}{\partial x_j}\right)_{,i} = \left[-\frac{\partial T}{\partial t}\frac{\partial u^i}{\partial x_2} + u^j g^{ik}(u_{j,k} - u_{k,j})\right]_{,i}. \tag{2.16}$$

2.2. *Discretization and the Iterative Method*

The solution $(\mathbf{u}, p)$ of (2.15) and (2.16) may be expressed in wave space as an approximation of (1.4) with the ranges of k_1, k_2, k_3 truncated to form a finite series of mode combinations [18–20]. The truncations are

$$\begin{aligned} k_1 &= 0, \frac{N_1}{2} - 1 \\ k_2 &= 0, N_2 - 1 \\ k_3 &= -\frac{N_3}{2} + 1, \frac{N_3}{2}. \end{aligned} \tag{2.17}$$

$N_{1,2,3}$ correspond to the total number of grid points in each of the three dimensions of discrete space. Likewise, the continuous operators in (2.15) are approximated by their discrete counterparts:

$$\begin{aligned} -\frac{\partial T}{\partial t}\frac{\partial u^i}{\partial x_2} + u^j g^{ik}(u_{j,k} - u_{k,j}) &\to \mathcal{N}(\hat{\mathbf{u}}) \\ g^{ij}\frac{\partial p}{\partial x_j} &\to \mathcal{G}(\hat{\mathbf{p}}) \\ \frac{1}{\mathrm{Re}}(g^{jk}u^i_{,k})_{,j} &\to \mathcal{L}(\hat{\mathbf{u}}). \end{aligned} \tag{2.18}$$

A circumflex (ˆ) denotes spectral representation. $\hat{p}(k_1, k_2, k_3, t)$ is a complex-valued vector of dimension $(N_1/2) \times N_2 \times N_3$; $\hat{\mathbf{u}}(k_1, k_2, k_3, t)$ is a complex-valued vector of dimension $3 \times (N_1/2) \times N_2 \times N_3$. $\mathcal{N}(\hat{\mathbf{u}})$, $\mathcal{G}(\hat{\mathbf{u}})$, and $\mathcal{L}(\hat{\mathbf{u}})$ represent the convective, gradient, and viscous terms, respectively. In discrete time, (2.15) becomes

$$\frac{\hat{\mathbf{u}}^{n+1} - \hat{\mathbf{u}}^n}{\delta t} = \mathcal{N}(\hat{\mathbf{u}}^n) - \mathcal{G}(\hat{\mathbf{p}}^{n+1/2}) + \frac{1}{\mathrm{Re}}\mathcal{L}(\hat{\mathbf{u}}^{n+1}). \tag{2.19}$$

n denotes position in time. The viscous term is treated implicitly (backward Euler) to preclude a severe restriction on stability. The convective term is treated explicitly using a Runge–Kutta scheme in which the term is advanced from position n to position $n + 1$ in three substeps. In order to present the iterative method with optimal clarity, a description of the fractional time step (and concomitant notation) is postponed until subsection 2.5. The time position for the pressure term $(n + \frac{1}{2})$ indicates that the term is treated neither explicitly nor implicitly in the conventional senses; it is computed so as to enforce the solenoidal condition on velocity at the latest position in time. The solenoidal condition is

$$\mathcal{D}(\hat{\mathbf{u}}^{n+1}) = 0; \tag{2.20}$$

$\mathcal{D}$ is the discrete divergence operator:

$$u^i_{,i} \to \mathcal{D}(\hat{\mathbf{u}}). \tag{2.21}$$

As the metric commutes under covariant differentiation, $\mathcal{D}$ commutes with $\mathcal{L}$:

$$\mathcal{D}[\mathcal{L}(\hat{\mathbf{u}}^{n+1})] = \mathcal{L}[\mathcal{D}(\hat{\mathbf{u}}^{n+1})] = 0. \tag{2.22}$$

$\mathcal{D}$ operating on (2.19), in conjunction with (2.20) and (2.22), yields the equation for pressure:

$$\mathcal{D}[\mathcal{G}(\hat{\mathbf{p}}^{n+1/2})] = \mathcal{D}[\mathcal{N}(\hat{\mathbf{u}}^n)]. \tag{2.23}$$

The left side of (2.23) is separated into an invertible part and the remainder. Returning for the moment to continuous form, the split is

$$\left(g^{ij}\frac{\partial p}{\partial x_j}\right)_{,i} = \frac{\partial^2 p}{\partial x_i\,\partial x_i} + \left[\left(g^{ij}\frac{\partial p}{\partial x_j}\right)_{,i} - \frac{\partial^2 p}{\partial x_i\,\partial x_i}\right]. \tag{2.24}$$

Denoting the discrete version of the invertible part as

$$\frac{\partial^2 p}{\partial x_i\,\partial x_i} \to \Delta\hat{\mathbf{p}}, \tag{2.25}$$

the equation for pressure becomes

$$\Delta\hat{\mathbf{p}}^{n+1/2}_{s+1} = \overbrace{\mathcal{D}[\mathcal{N}(\hat{\mathbf{u}}^n)]}^{1} + \overbrace{\Delta\hat{\mathbf{p}}^{n+1/2}_s - \mathcal{D}[\mathcal{G}(\hat{\mathbf{p}}^{n+1/2}_s)]}^{2}, \tag{2.26}$$

where s denotes position in an iterative sequence; (2.26) is equivalent to (2.23) in the limit as $\hat{\mathbf{p}}_{s+1} \to \hat{\mathbf{p}}_s$. The viscous operator in (2.19) is split in an analogous manner:

$$\mathcal{L}(\hat{\mathbf{u}}) = \Delta\hat{\mathbf{u}} + [\mathcal{L}(\hat{\mathbf{u}}) - \Delta(\hat{\mathbf{u}})]. \tag{2.27}$$

And the evolution equation may also be expressed as an iterative sequence:

$$\left(I - \frac{\delta t}{\mathrm{Re}}\Delta\right)\hat{\mathbf{u}}_{s+1}^{n+1} = \overbrace{\hat{\mathbf{u}}^n + \delta t\,[\mathcal{N}(\hat{\mathbf{u}}^n)]}^{1} + \overbrace{\frac{\delta t}{\mathrm{Re}}(\mathcal{L} - \Delta)(\hat{\mathbf{u}}_s^{n+1}) - \delta t\,[\mathcal{G}(\hat{\mathbf{p}}_{s+1}^{n+1/2})]}^{2}; \quad (2.28)$$

(2.28) is equivalent to (2.19) in the limit as $\hat{\mathbf{u}}_{s+1} \to \hat{\mathbf{u}}_s$. Parts 1 in (2.26) and (2.28) are computed once at the beginning of each time step (and remain fixed during the iteration sequence); parts 2 are updated after each iteration until the solution converges. In wave space the operator Δ is

$$\Delta = \kappa + D^2 \quad (2.29)$$

$$\kappa \equiv -4\pi^2\left[\left(\frac{k_1}{L_1}\right)^2 + \left(\frac{k_3}{L_3}\right)^2\right]; \quad (2.30)$$

D^2 is the discrete representation of the second derivative (in x_2) operator. In connection with the three-substep Runge–Kutta method, subsection 2.5 identifies the relative weight apportioned to δt in each term in (2.28) at each substep.

At each position in time n and in the iterative sequence s, for each Fourier mode combination k_1, k_3, (2.26) and (2.28) form a set of one-dimensional Helmholtz equations:

$$(D^2 + \lambda_1)\hat{\mathbf{p}} = \hat{\mathbf{f}}_1 \quad (2.31)$$

$$(D^2 + \lambda_2)\hat{\mathbf{u}} = \hat{\mathbf{f}}_2 \quad (2.32)$$

$$\lambda_1 \equiv \kappa; \quad \lambda_2 \equiv \kappa - \frac{\mathrm{Re}}{\delta t}; \quad (2.33)$$

$\hat{\mathbf{f}}_{1,2}$ are the right sides of (2.26) and (2.28), respectively. These functions are known, consisting in general of products of derivatives of $\hat{\mathbf{u}}$ and $\hat{\mathbf{p}}$ and the metric coefficients. They are computed in a multistep process: differentiation in wave space, multiplication by collocation in physical space with Fast Fourier Transformations (FFT) at each intermediate level. Multiplication in physical space couples all Fourier modes of the solution within the iterative sequence. The equations for pressure and velocity are elliptic. Taking in aggregate the subsystems corresponding to each Fourier mode combination, separation of terms into the invertible part and a remainder is equivalent to a Richardson iteration method with a relaxation parameter of unity and preconditioning, the preconditioning operators being Δ^{-1} for pressure and $(\Delta - (\mathrm{Re}/\delta t)I)^{-1}$ for velocity.

The evolution equation for velocity (2.32) is separated into an equation for each directional component of the vector, coupled within the iterative sequence through the viscous terms in $\hat{\mathbf{f}}_2$. Thus, the system (2.31) and (2.32) becomes a set of four Helmholtz equations for each k_1, k_3, s, n combination. The solution $(\hat{\mathbf{u}}, \hat{\mathbf{p}})$ is a set of N_2-dimensional vectors.

In discrete Chebyshev space, the operator $(D^2 + \lambda)$ in (2.31) and (2.32) forms a loosely banded pentadiagonal system of dimensions $N_2 \times N_2$. Replacing two rows with prescriptions for the boundary conditions determines the system. An equivalent, more efficient form may be constructed consisting of two tridiagonal systems, one for the even Chebyshev modes, one for the odd.

2.3. *Boundary Conditions*

In general, displacement of the lower wall constitutes a change in the control volume. And with periodic conditions in the stream- and spanwise directions (no net mass flux), the solenoidal condition mandates that fluid be added or extracted through the upper wall at a rate commensurate with the velocity of the lower wall ($\tilde{u}^2|_{x_2=\pm 1} = \partial h/\partial t$). The horizontal components of velocity are zero at both walls. Therefore, the prescribed boundary conditions for velocity (in the computational frame) are

$$\begin{aligned} u^1|_{x_2=\pm 1} &= 0 \\ u^2|_{x_2=\pm 1} &= \left(\frac{\partial T}{\partial x_2}\right)^{-1}\left(\frac{\partial h}{\partial t}\right) \\ u^3|_{x_2=\pm 1} &= 0. \end{aligned} \quad (2.34)$$

Boundary conditions for pressure are determined indirectly from the solenoidal condition via an influence matrix technique. The divergence of velocity (in continuous form) is

$$u_{,i}^i = \frac{\partial u^1}{\partial x_1} + \frac{\partial u^2}{\partial x_2} + \frac{\partial u^3}{\partial x_3} + \left(\frac{\partial T}{\partial x_2}\right)^{-1} \cdot \left[u^1\left(\frac{\partial^2 T}{\partial x_1\,\partial x_2}\right) + u^3\left(\frac{\partial^2 T}{\partial x_2\,\partial x_3}\right)\right] = 0. \quad (2.35)$$

The boundary conditions on u^1 and u^3 along with (2.35) yield

$$\left.\frac{\partial u^2}{\partial x_2}\right|_{x_2=\pm 1} = 0. \quad (2.36)$$

These conditions correspond exactly to those of the canonical channel and the same methods may be brought to bear (with some modification) [21]. The idea is to find boundary conditions for pressure which enforce (2.36). Returning to discrete wave space, the following relations are defined for pressure and the second component of velocity (denoted here as $\hat{\mathbf{v}}$):

$$\hat{\mathbf{p}} = \hat{\mathbf{p}}_p + c_1\hat{\mathbf{p}}_1 + c_2\hat{\mathbf{p}}_2 \quad (2.37)$$

$$\hat{\mathbf{v}} = \hat{\mathbf{v}}_p + c_1\hat{\mathbf{v}}_1 + c_2\hat{\mathbf{v}}_2. \quad (2.38)$$

The constants $c_{1,2}$ are independent of x_2 and therefore depend

only upon k_1, k_3. For each Fourier mode combination, a pair of constants which satisfies the following two-dimensional system will define a $\hat{\mathbf{v}}$ which satisfies (2.36):

$$\begin{pmatrix} c_1 \\ c_2 \end{pmatrix} = -\begin{pmatrix} D\hat{\mathbf{v}}_1|_{x_2=+1} & D\hat{\mathbf{v}}_2|_{x_2=+1} \\ D\hat{\mathbf{v}}_1|_{x_2=-1} & D\hat{\mathbf{v}}_2|_{x_2=-1} \end{pmatrix}^{-1} \begin{pmatrix} D\hat{\mathbf{v}}_p|_{x_2=+1} \\ D\hat{\mathbf{v}}_p|_{x_2=-1} \end{pmatrix}; \quad (2.39)$$

D is the discrete representation of the first derivative (in x_2) operator:

$$\frac{\partial}{\partial x_2} \rightarrow D. \quad (2.40)$$

The wall-normal component of the gradient operator may be split into an operator D which commutes with $c_{1,2}$ and the remainder:

$$R(\hat{\mathbf{p}}) = [\mathcal{G}(\hat{\mathbf{p}})] \cdot \mathbf{e}_2 - D(\hat{\mathbf{p}}). \quad (2.41)$$

The separate solutions $(\hat{\mathbf{v}}, \hat{\mathbf{p}})_{p,1,2}$ must collectively satisfy the original equations for pressure and velocity. In order to consolidate terms, parts 1 of (2.26) and (2.28) are, respectively,

$$\hat{\mathbf{r}}_1 \equiv \mathcal{D}[\mathcal{N}(\hat{\mathbf{u}}^n)] \quad (2.42)$$

$$\hat{\mathbf{r}}_2 \equiv \hat{\mathbf{u}}^n + \delta t[\mathcal{N}(\hat{\mathbf{u}}^n)]. \quad (2.43)$$

$\hat{\mathbf{r}}_{1,2}$ are computed from values of the solution at time position n and they are not iterated upon; the remaining terms (parts 2) are computed from values at time position $n + 1$ (via the iterative sequence). Dropping the time position notation in these remaining terms in (2.26) and (2.28), the equations for pressure and the second component of velocity are

$$\Delta\hat{\mathbf{p}}^{s+1} = \hat{\mathbf{r}}_1 + \Delta\hat{\mathbf{p}}^s - \mathcal{D}[\mathcal{G}(\hat{\mathbf{p}}^s)] \quad (2.44)$$

$$\left(I - \frac{\delta t}{\mathrm{Re}}\Delta\right)\hat{\mathbf{v}}^{s+1} = \left[\hat{\mathbf{r}}_2 + \frac{\delta t}{\mathrm{Re}}(\mathcal{L} - \Delta)(\hat{\mathbf{u}}^s)\right] \cdot \mathbf{e}_2 - \delta t\,[(D + R)(\hat{\mathbf{p}}^{s+1})]. \quad (2.45)$$

Noting that Δ commutes with $c_{1,2}$, equations for $(\hat{\mathbf{v}}, \hat{\mathbf{p}})_{p,1,2}$ which satisfy (2.44) and (2.45) are

$$\Delta\hat{\mathbf{p}}_p^{s+1} = \hat{\mathbf{r}}_1 + \Delta\hat{\mathbf{p}}_p^s - \mathcal{D}[\mathcal{G}(\hat{\mathbf{p}}_p^s + c_1^s\hat{\mathbf{p}}_1 + c_2^s\hat{\mathbf{p}}_2)] \quad (2.46)$$

$$\Delta\hat{\mathbf{p}}_1 = 0 \quad (2.47)$$

$$\Delta\hat{\mathbf{p}}_2 = 0 \quad (2.48)$$

$$\left(I - \frac{\delta t}{\mathrm{Re}}\Delta\right)\hat{\mathbf{v}}_p^{s+1} = \left[\hat{\mathbf{r}}_2 + \frac{\delta t}{\mathrm{Re}}\mathcal{L}(\hat{\mathbf{u}}^s)\right] \cdot \mathbf{e}_2 - \delta t\left[\frac{1}{\mathrm{Re}}\Delta\hat{\mathbf{v}}_p^s + D(\hat{\mathbf{p}}_p^{s+1})\right] + \delta t[R(\hat{\mathbf{p}}_p^{s+1} + c_1^s\hat{\mathbf{p}}_1 + c_2^s\hat{\mathbf{p}}_2)] \quad (2.49)$$

$$\left(I - \frac{\delta t}{\mathrm{Re}}\Delta\right)\hat{\mathbf{v}}_1 = -\delta t[D(\hat{\mathbf{p}}_1)] \quad (2.50)$$

$$\left(I - \frac{\delta t}{\mathrm{Re}}\Delta\right)\hat{\mathbf{v}}_2 = -\delta t[D(\hat{\mathbf{p}}_2)] \quad (2.51)$$

The solutions $(\hat{\mathbf{v}}, \hat{\mathbf{p}})_{1,2}$ are not iterated upon; however, the constants $c_{1,2}$ are, so that the boundary conditions (2.36) are enforced at each position in the iterative sequence. Boundary conditions for the separate solutions of wall-normal velocity (for each Fourier mode combination) are

$$\begin{aligned} \hat{\mathbf{v}}_p|_{x_2=\pm 1} &= \hat{\mathbf{u}}^2|_{x_2=\pm 1} \\ \hat{\mathbf{v}}_1|_{x_2=\pm 1} &= 0 \\ \hat{\mathbf{v}}_2|_{x_2=\pm 1} &= 0, \end{aligned} \quad (2.52)$$

and boundary conditions for the separate solutions of pressure (for each Fourier mode combination) are

$$\begin{aligned} &\hat{\mathbf{p}}_p|_{x_2=+1} = 0; \quad \hat{\mathbf{p}}_p|_{x_2=-1} = 0 \\ &\hat{\mathbf{p}}_1|_{x_2=+1} = 0; \quad \hat{\mathbf{p}}_1|_{x_2=-1} = 1 \\ &\hat{\mathbf{p}}_2|_{x_2=+1} = 1; \quad \hat{\mathbf{p}}_2|_{x_2=-1} = 0. \end{aligned} \quad (2.53)$$

The conditions on $\hat{\mathbf{p}}_{1,2}$ ensure that a solution exists for each $c_{1,2}$: the determinant of the influence matrix in (2.39) is guaranteed to be non-zero. For the zeroth Fourier mode combination ($k_{1,3} = 0$) the equations for $\hat{\mathbf{p}}_{1,2}$, (2.47) and (2.48), reduce to $D^2(\hat{\mathbf{p}}_{1,2}) = 0$. The influence matrix determinant is then zero for *any* boundary conditions on $\hat{\mathbf{p}}_{1,2}$, guaranteeing that *no* nontrivial solution exists for $c_{1,2}$: the method breaks down. This problem vanishes in the case of the canonical channel because the solenoidal condition mandates that mean wall-normal velocity is zero everywhere in the domain.

Under the coordinate transformation, mean wall-normal velocity is, in general, non-zero and must be computed (in some way other than the influence matrix method). Mean pressure is determined from the divergence of the Navier–Stokes equation (2.46), using the boundary conditions for $\hat{\mathbf{p}}_p$ (2.53) and $c_{1,2} = 0$. Mean wall-normal velocity is determined directly from the solenoidal condition:

$$\left\langle \frac{\partial u^2}{\partial x_2} \right\rangle = -\left\langle \left(\frac{\partial T}{\partial x_2}\right)^{-1}\left[u^1\left(\frac{\partial^2 T}{\partial x_1\,\partial x_2}\right) + u^3\left(\frac{\partial^2 T}{\partial x_2\,\partial x_3}\right)\right]\right\rangle. \quad (2.54)$$

The bracket $\langle\ \rangle$ denotes a mean quantity. Two boundary conditions are required for $\langle u^2 \rangle$. Because mean pressure and wall-normal velocity are each computed from equations which contain the incompressibility information, replacement of two rows (rather than one) in the system corresponding to (2.54) with two boundary conditions (rather than one) does not compromise the divergence-free condition.

The equation for mean pressure (2.46) is obtained from the divergence of the Navier–Stokes equation, part of which comes from the first derivative (D) of the wall-normal component of that equation (2.49). Through this operation the row corresponding to the zeroth Chebyshev mode in (2.49) drops out and the information is lost. Mean wall-normal velocity is computed from the continuity equation (2.54) which contains no information from the Navier–Stokes equation. Therefore, the wall-normal component of the Navier–Stokes equation is not satisfied for $k_{1,2,3} = 0$. All other Chebyshev modes of the mean wall-normal component (and all modes of the mean stream- and spanwise components) of the equation are satisfied. The solenoidal condition is enforced exactly for all Chebyshev modes. Exact enforcement of the solenoidal condition for the higher Fourier modes is described in the next section.

2.4. *The Tau Correction*

The influence matrix method effectively uncouples the equations for $\hat{\mathbf{p}}$ from those for $\hat{\mathbf{u}}$. In wave space the Helmoltz equations for pressure and velocity, for each k_1,k_3, s, n combination, consist of two tridiagonal systems, one for the even Chebyshev modes and one for the odd. The boundary conditions for each pressure and velocity solution uncouple as well, into one equation for the even modes and one for the odd. The odd/even boundary condition equations, which are full rows in matrix form, replace the rows corresponding to the highest Chebyshev mode in the odd/even tridiagonal systems. Each of the solutions then has associated with it two errors, τ^{N_2-2,N_2-1}, incurred by the replacements. The equation for pressure is obtained from the divergence of the evolution equation (and imposition of the solenoidal condition on velocity). In the case of the canonical channel, the divergence of any vector $\hat{\mathbf{r}}$ is

$$\mathcal{D}(\hat{\mathbf{r}}) = \frac{2\pi i k_1}{L_1}\hat{r}^1 + D(\hat{r}^2) + \frac{2\pi i k_3}{L_3}\hat{r}^3. \tag{2.55}$$

Errors τ^{N_2-2,N_2-1} in the systems for wall-normal velocity are propagated by the derivative operator D into all modes in the systems for pressure. And because the solution is computed sequentially ($\hat{\mathbf{p}} \rightarrow \hat{\mathbf{v}}$) via the influence matrix method, pressure no longer enforces the solenoidal condition. For the simple channel, a tau correction method has been devised to circumvent the problem [20, 21]. Fortunately, the divergence operator in the curvilinear coordinate frame (2.35) propagates these errors in exactly the same manner, so that the technique may be used without modification. Summarizing the method, a tau solution is defined by the following set of equations:

$$(D^2 + \lambda_1)\hat{\mathbf{p}}_\tau = \hat{\mathbf{f}} \tag{2.56}$$

$$(D^2 + \lambda_2)\mathbf{v}_\tau \Rightarrow \frac{\mathbf{Re}}{\delta t}[D(\hat{\mathbf{p}}_\tau)]; \tag{2.57}$$

$\hat{\mathbf{p}}_\tau$ and $\hat{\mathbf{v}}_\tau$ are zero at the walls. The parameters $\lambda_{1,2}$ are defined by (2.33). The right side of (2.56) is defined as

$$f^{k_2} \equiv \frac{2}{c^{k_2}}k_2'; \quad c^{k_2} = \begin{cases} 2 & (k_2 = 0) \\ 1 & (k_2 \neq 0) \end{cases};$$
$$k_2' = \begin{cases} N_2 - 2 & (k_2 \text{ even}) \\ N_2 - 1 & (k_2 \text{ odd}) \end{cases}. \tag{2.58}$$

And with $\tau_{p,1,2}^{N_2-2,N_2-1}$ denoting the tau errors in the systems for $\hat{\mathbf{v}}_{p,1,2}$ the corrected solutions are

$$\hat{\mathbf{p}}_{p,1,2}^{k_2} = \hat{\mathbf{p}}_{p,1,2}^{k_2} + \tau_{p,1,2}^{k_2'}\hat{\mathbf{p}}_\tau^{k_2} \tag{2.59}$$

$$\hat{\mathbf{v}}_{p,1,2}^{k_2} = \hat{\mathbf{v}}_{p,1,2}^{k_2} + \tau_{p,1,2}^{(k_2'+1)'}\hat{\mathbf{v}}_\tau^{k_2}. \tag{2.60}$$

The new wall-normal velocities satisfy modes 0 through $N_2 - 3$ of the original equations, and they satisfy the original equations (with the tau error) at the two highest modes. The new pressures enforce the solenoidal condition at modes 0 through $N_2 - 3$. With enforcement on the boundaries the velocity field is exactly solenoidal. The solutions $(\hat{\mathbf{v}}, \hat{\mathbf{p}})_\tau$ are not iterated upon; however, the tau errors $\tau_p^{N_2-2,N_2-1}$ are, so that the solenoidal condition is enforced at each position in the iterative sequence. Figure 2, a flowchart of the entire algorithm with equation numbers referenced, distinguishes clearly which terms lie within the iterative loop and which do not.

2.5. *Time Integration*

Velocity in the evolution equation is advanced in time by means of a three-substep Runge–Kutta method [22]. While the viscous term is fully implicit in time, it is treated semi-implicitly within the context of the iterative sequence. However, the method of time integration may be described most clearly by dispensing with the fact that an iterative sequence exists and considering only advancement from the converged solution at time position n to the converged solution at time position $n + 1$. Denoting the quantity to be advanced as u, the representative evolution equation is

$$\frac{\partial u}{\partial t} = -G_r(p, t) + L(u, t) + N(u, t); \tag{2.61}$$

$G_r(p, t)$, $L(u, t)$, and $N(u, t)$ are the pressure gradient, viscous, and convective terms, respectively. Through the time dependence of the coordinate transformation, all of the terms depend explicitly upon time. The discrete version of the equation is

$$\frac{u^{n+1} - u^n}{\Delta t} = -G_r(p^{n+1/2}, t^{n+1}) + L(u^{n+1}, t^{n+1}) + N(u^n, t^{n+1}). \tag{2.62}$$

As a compromise between storage limitations and accuracy, a Runge–Kutta method is employed in which only one previous substep term has to be saved. The solution is advanced from position n to position $n + 1$ in three substeps:

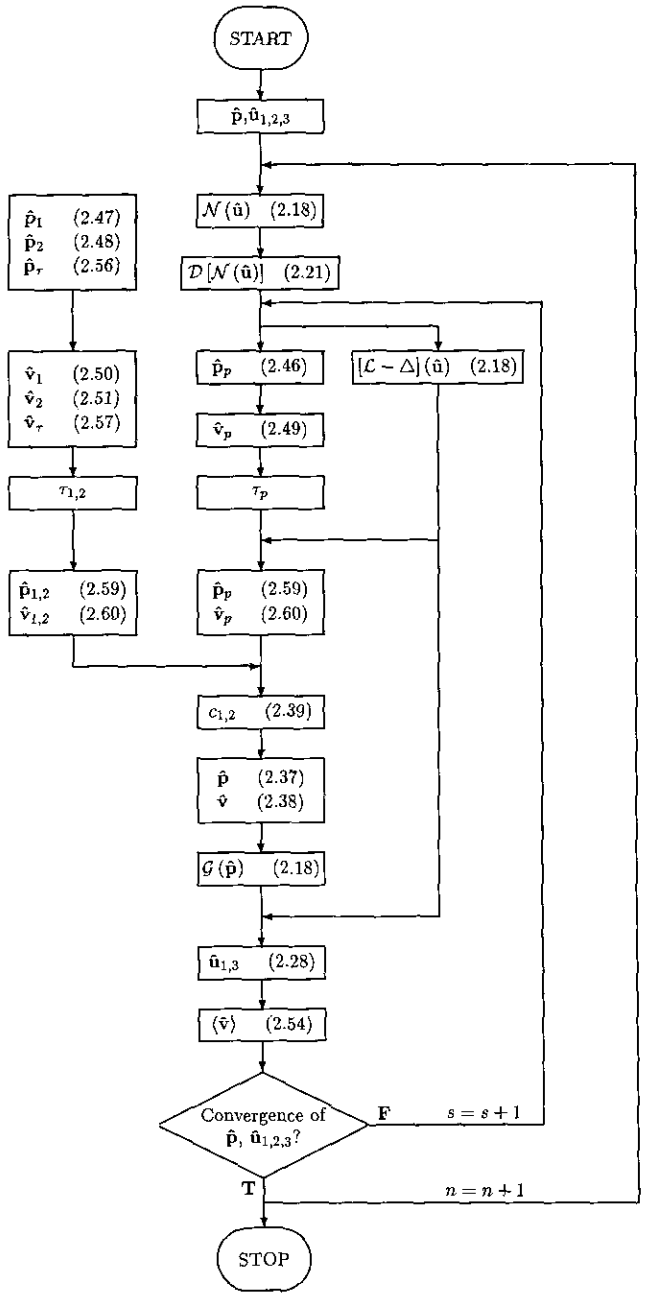

FIG. 2. A flowchart of the algorithm. The equation corresponding to each computed term is referenced by number. Note that because $v_{1,2}$ depend upon Δt, these solutions must be placed within the time sequence, but still outside the iteration sequence, when using the variable step size mode.

$$
\begin{aligned}
u^{i} &= u^{n} + \Delta t\,[-\alpha_1 G_r^{i} + \gamma_1 L^{i} + \zeta_1 N^{n}] \\
u^{ii} &= u^{i} + \Delta t\,[-\alpha_2 G_r^{ii} - \beta_1 G_r^{i} + \gamma_2 L^{ii} + \zeta_2 N^{i} + \eta_1 N^{n}] \\
u^{n+1} &= u^{ii} + \Delta t\,[-\alpha_3 G_r^{n+1} - \beta_2 G_r^{ii} + \gamma_3 L^{n+1} + \zeta_3 N^{ii} + \eta_2 N^{i}].
\end{aligned} \tag{2.63}
$$

The following relations enforce the solenoidal condition at each substep:

TABLE I

R-K step	Δt	α	β	γ	ζ	η	ξ
i	$\frac{8}{15}$	$\frac{8}{15}$	—	$\frac{8}{15}$	$\frac{8}{15}$	—	0
ii	$\frac{2}{15}$	$\frac{5}{12}$	$-\frac{17}{60}$	$\frac{2}{15}$	$\frac{5}{15}$	$-\frac{17}{60}$	$\frac{8}{15}$
iii	$\frac{1}{3}$	$\frac{3}{4}$	$-\frac{5}{12}$	$\frac{1}{3}$	$\frac{3}{4}$	$-\frac{5}{12}$	$\frac{2}{15}$

$$
\begin{aligned}
\alpha_1 &= \zeta_1; \quad \beta_1 = \eta_1 \\
\alpha_2 &= \zeta_2; \quad \beta_2 = \eta_2 \\
\alpha_3 &= \zeta_3.
\end{aligned} \tag{2.64}
$$

The independent variable t, explicit in all the terms, is advanced in an analogous manner:

$$
\begin{aligned}
t^{i} &= t^{n} + \Delta t\,\xi_1 \\
t^{ii} &= t^{i} + \Delta t\,\xi_2 \\
t^{n+1} &= t^{ii} + \Delta t\,\xi_3.
\end{aligned} \tag{2.65}
$$

The sizes of each substep for the viscous term and the sizes for the convective and gradient terms are made equivalent by the following relations:

$$
\begin{aligned}
\Delta t^{i} &= \alpha_1 = \gamma_1 \\
\Delta t^{ii} &= \alpha_2 + \beta_1 = \gamma_2 \\
\Delta t^{iii} &= \alpha_3 + \beta_2 = \gamma_3
\end{aligned} \tag{2.66}
$$

$$
\Delta t^{i} + \Delta t^{ii} + \Delta t^{iii} = \Delta t. \tag{2.67}
$$

With the lower wall accelerating the boundary conditions become explicitly dependent upon time. Denoting wall-normal velocity at the walls as v and a constant acceleration as a, the boundary conditions are advanced in time as follows:

$$
\begin{aligned}
v^{i} &= v^{n} + a\,\Delta t^{i} \\
v^{ii} &= v^{i} + a\,\Delta t^{ii} \\
v^{iii} &= v^{ii} + a\,\Delta t^{iii}.
\end{aligned} \tag{2.68}
$$

Equations for the parameters are derived by Taylor expanding (2.62), Taylor expanding (2.63), and matching terms. Values of the parameters are given in Table I.

The purely viscous and two of the mixed viscous-convective terms of order $(\Delta t)^3$ cannot be matched: for low Reynolds number flows the error is approximately $(\Delta t)^3$. In the limit as the Reynolds number approaches infinity, the error approaches $(\Delta t)^4$. The stability condition is based upon the explicit time step and is determined by a conventionally defined CFL number:

$$
\mathrm{CFL} = \pi \left[\frac{|u^1|}{\Delta x_1} + \frac{|u^2|}{\Delta x_2} + \frac{|u^3|}{\Delta x_3} \right] \Delta t; \tag{2.69}
$$

TABLE II

Flow parameters	Box dimensions	No. grid points
Re = 100	$L_1 = 4\pi$	$N_1 = 16$
$C = 0.75$	$L_2 = 2$	$N_2 = 17$
$\varepsilon = 0.075$	$L_3 = 2\pi$	$N_3 = 16$

Note. See Figs. 3 and 4.

$\Delta x_{1,2,3}$ are the grid spacings. The theoretical limit of the CFL number is $\sqrt{3}$. Two modes of operation are available. In a fixed mode the time step size is specified at the onset and remains constant. In a variable mode the step size finds its maximum based on the stability condition: Δt is derived from (2.69) using the CFL limit.

3. TESTING

This section contains a description of all testing including the benchmark tests which validate canonical channel flow simulations, the static and dynamic tests of one-dimensional non-canonical channel flows, the two- and three-dimensional Stokes flows across perturbed walls, and the separated flow over a three-dimensional protuberance.

3.1. *The Canonical Channel*

First is a test of the stability of Poiseuille flow in a flat-walled channel at a low Reynolds number (Table II). Stability is confirmed and the decay rate of mean flow perturbations is compared with results from the same test conducted by Yang [23]. The initial velocity field is

$$\begin{aligned} u_1(x_1, x_2, x_3) &= C(1 - x_2^8) \\ &\quad + \epsilon \frac{L_1}{2} \sin(\pi x_2) \cos\left(\frac{4\pi x_1}{L_1}\right) \sin\left(\frac{2\pi x_3}{L_3}\right) \\ u_2(x_1, x_2, x_3) &= -\epsilon[1 + \cos(\pi x_2)] \sin\left(\frac{4\pi x_1}{L_1}\right) \sin\left(\frac{2\pi x_3}{L_3}\right) \\ u_3(x_1, x_2, x_3) &= -\epsilon \frac{L_3}{2} \sin\left(\frac{4\pi x_1}{L_1}\right) \sin(\pi x_2) \cos\left(\frac{2\pi x_3}{L_3}\right). \end{aligned} \tag{3.1}$$

Flow should converge to a parabolic profile:

$$U_1(x_2) = 1 - x_2^2. \tag{3.2}$$

The flow is maintained by imposing first a constant mean streamwise pressure gradient (Fig. 3) and second a constant streamwise mass flux (Fig. 4). Yang's algorithm is also pseudospectral and uses a hybrid method of time integration, but with a Crank–Nicholson prescription for the viscous term and an Adams–Bashforth for the nonlinear (as opposed to Backward Euler and Runge–Kutta). Notwithstanding these differences, the convergence rates are almost identical. As is evident from a comparison of the rates of Fig. 4 with those of Fig. 3, constant mass flux makes for a more robust flow.

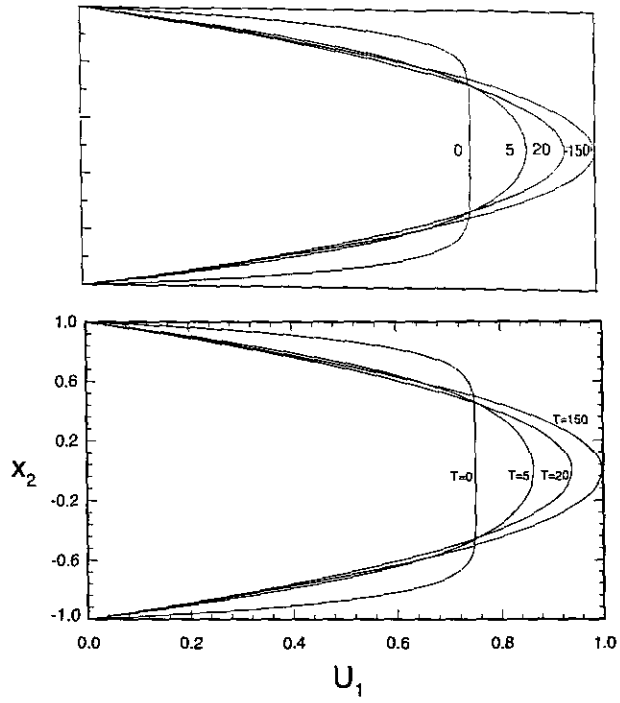

FIG. 3. Stability of low Reynolds number Poiseuille flow in a flat-walled channel (Table II) with a constant mean streamwise pressure gradient. Shown are profiles of mean streamwise velocity at times $T = 0, 5, 20, 150$ (bottom) and results of an identical test conducted by Yang [23] (top).

Second is a test of the decay rate of small amplitude disturbances in a plane-parallel shear flow: comparison of values obtained by direct simulation with values derived from the Orr–Sommerfeld equation. The mean flow is parabolic and disturbances may be either two- or three-dimensional. The streamwise perturbation velocity is

$$u_1'(x_1, x_2, x_3, t) = \epsilon \rho_1(x_2) e^{\gamma_i t} \cos[\alpha x_1 + \beta x_3 - \gamma_r t + \phi_1(x_2)]; \tag{3.3}$$

α and β correspond to the Fourier modes of the chosen disturbance. Given a sufficiently small initial perturbation ε, an eigenvalue problem is derived from the Navier–Stokes equation by normal mode and linear stability methods [24, 25]. $\rho_1(x_2)$ and $\phi_1(x_2)$ are the eigenfunctions in polar form, $\gamma = \gamma_r + i\gamma_i$ the eigenvalues. Using computed eigenfunctions the amplitude decay rate γ_i and the rate of phase change γ_r may be calculated

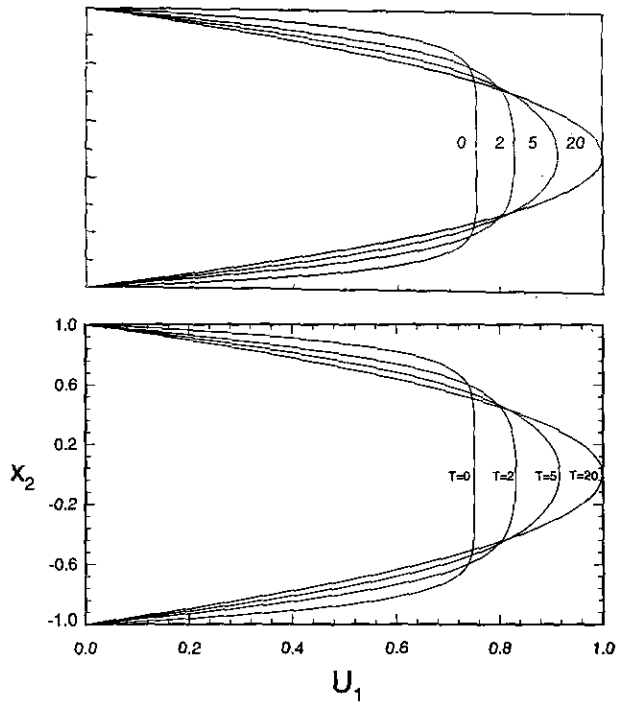

FIG. 4. Stability of low Reynolds number Poiseuille flow in a flat-walled channel (Table II with a constant streamwise mass flux. Shown are profiles of mean streamwise velocity at times $T = 0, 2, 5, 20$ (bottom) and results of an identical test conducted by Yang [23] (top).

from the Orr–Sommerfeld equation and compared with values from the direct simulation, which are determined from the streamwise velocity:

$$u_1(x_1, x_2, x_3, t) = 2a_1(x_2, t)\cos(\alpha x_1 + \beta x_3) - 2b_1(x_2, t)\sin(\alpha x_1 + \beta x_3); \tag{3.4}$$

(a_1, b_1) is the Fourier coefficient, real and imaginary part, corresponding to the perturbed mode. In polar form (3.4) becomes

$$\begin{aligned} u_1(x_1, x_2, x_3, t) &= r_1(x_2, t)\cos[\alpha x_1 + \beta x_3 + \theta_1(x_2, t)] \\ r_1(x_2, t) &= 2[a_1(x_2, t)^2 + b_1(x_2, t)^2]^{1/2} \\ \theta_1(x_2, t) &= \tan^{-1}\left[\frac{b_1(x_2, t)}{a_1(x_2, t)}\right]. \end{aligned} \tag{3.5}$$

The amplitude decay rate γ_i is determined by equating (3.3) and (3.5):

$$u_1^2 + \left(\alpha^{-1}\frac{\partial u_1}{\partial x_1}\right)^2 = (u_1')^2 + \left(\alpha^{-1}\frac{\partial u_1'}{\partial x_1}\right)^2 = [\epsilon\rho_1(x_2)]^2 e^{2\gamma_i t} \tag{3.6}$$

TABLE III

Flow parameters	Wave number	Box dimensions	No. grid points
Re = 1500	$\alpha = 1$	$L_1 = 2\pi$	$N_1 = 16$
$\epsilon = 2.198 \times 10^{-5}$	$\beta = 0$ (2D)	$L_2 = 2$	$N_2 = 33$
	$\beta = -1$ (3D)	$L_3 = 2\pi$	$N_3 = 16$

$$\gamma_i = -\frac{1}{2T}\ln\left(\frac{[u_1(x_2, 0)]^2 + \left[\alpha^{-1}\dfrac{\partial u_1(x_2, 0)}{\partial x_1}\right]^2}{[u_1(x_2, T)]^2 + \left[\alpha^{-1}\dfrac{\partial u_1(x_2, T)}{\partial x_1}\right]^2}\right) - 2(\ln[\epsilon\rho_1(x_2)] - \ln[\epsilon\rho_1(x_2)]) \tag{3.7}$$

$$\gamma_i = -\frac{1}{2T}\ln\left[\frac{a_1^2(x_2, 0) + b_1^2(x_2, 0)}{a_1^2(x_2, T) + b_1^2(x_2, T)}\right]. \tag{3.8}$$

The rate of phase change γ_r is determined similarly:

$$\frac{-\alpha^{-1}\dfrac{\partial u_1}{\partial x_1}}{u_1} = \tan[\alpha x_1 + \beta x_3 + \theta(x_2, t)] = \tan[\alpha x_1 + \beta x_3 + \phi(x_2) - \gamma_r t] \tag{3.9}$$

$$\gamma_r = \frac{1}{T}\left(\tan^{-1}\left[\frac{b_1(x_2, 0)}{a_1(x_2, 0)}\right] - \tan^{-1}\left[\frac{b_1(x_2, T)}{a_1(x_2, T)}\right]\right). \tag{3.10}$$

Each disturbance evolves from an initial time 0 to any arbitrary time T. Parameter values are listed in Table III.

For the two-dimensional disturbance, predicted values of γ_i and γ_r are -0.2820 and 0.3263, respectively. Relative errors in the computed values range from 0.05% in the middle third of the channel to 0.6% near the walls. For the three-dimensional disturbance, predicted values of γ_i and γ_r are -0.2823 and 0.4013. Relative errors in the computed values range from 0.07% in the middle third of the channel to 2.5% near the walls.

3.2. *The Non-canonical Channel: One-Dimensional Flows*

3.2.1. *Static tests.* In the first test of the coordinate transformation, the domain is defined by a flat wall at the top and a bottom wall which varies sinusoidally in the spanwise direction (invariant in time and in the streamwise direction). The perturbation of the bottom wall is

$$h(x_3 = \epsilon\sin\left(\frac{2\pi x_3}{L_3}\right). \tag{3.11}$$

In the limit as $\mathrm{Re} \to 0$, the convective term in the Navier–Stokes equation becomes negligible (Stokes flow). With no streamwise

TABLE IV

Flow/wall parameters	Time parameters	Box dimensions	No. grid points
$Re = 2$	$\Delta t \approx 0.1$	$L_1 = \pi$	$N_1 = 16$
$\varepsilon = 0.12$	$T = 10$	$L_2 = 2$	$N_2 = 33$
$\dot{\varepsilon} = 0$		$L_3 = \pi$	$N_3 = 32$

TABLE V

Flow/wall parameters	Time parameters	Box dimensions	No. grid points
$Re = 2$	$\Delta t \approx 0.1$	$L_1 = \pi$	$N_1 = 16$
$\varepsilon_* = 0.12$	$T \approx 30$	$L_2 = 2$	$N_2 = 33$
$\dot{\varepsilon}_*, \ddot{\varepsilon}_* = 0.01$		$L_3 = \pi$	$N_3 = 32$

Note. See Fig. 5.

dependence the Navier–Stokes equation admits a steady solution to the following Poisson equation (in Euclidian space):

$$\frac{\partial^2 u_1}{\partial \tilde{x}_2^2} + \frac{\partial^2 u_1}{\partial \tilde{x}_3^2} = \mathrm{Re}\left\langle \frac{\partial p_1}{\partial \tilde{x}_1} \right\rangle; \tag{3.12}$$

$\langle \partial p_1/\partial \tilde{x}_1 \rangle$ is the prescribed mean streamwise pressure gradient. In the computational frame the metric tensor complicates the equation considerably. However, a numerical solution is obtained by representing the streamwise velocity $\hat{\mathbf{u}}_1$ in wave space and constructing a linear system:

$$\mathbf{A}\hat{\mathbf{u}}_1 = \mathbf{f}. \tag{3.13}$$

Each row in the vector $\mathbf{A}\hat{\mathbf{u}}_1$ corresponds to the left side of (3.12) at a specific grid location in the two-dimensional domain. Because of the one-to-one correspondence between the number of grid points and the number of Fourier–Chebyshev modes, the system is determined: dimensions of the matrix $\mathbf{A}$ are $(N_2 \times N_3)^2$. $\hat{\mathbf{u}}_1$ and $\mathbf{f}$ are $(N_2 \times N_3)$-dimensional vectors. Rows in the system corresponding to grid locations on the boundaries are replaced with the boundary conditions, $\hat{\mathbf{u}}_1|_{x_2=\pm 1} = 0$. Using the numerical solution as an initial condition, flow is advanced in time to verify the steady solution. See Table IV.

After 10 time units (100 steps), the solution remains within round-off error (10^{-13}) of the initial condition. Spectral accuracy is obtained: the error is that incurred by the FFT subroutines. As a comparison the error in a second-order finite difference solution using the same spatial resolution would be of order 10^{-3}.

In all of the tests that follow a flat wall is perturbed in time to a specified configuration and height. With the target height, a maximum velocity, and a set acceleration (deceleration) as input, a controller adjusts the acceleration (turns it on or off or changes its sign) to ensure that the maximum velocity is not exceeded and that the wall arrives at its target height with zero velocity.

$$\varepsilon_* \Rightarrow \text{target height}$$

$$\dot{\varepsilon}_* \Rightarrow \text{maximum velocity}$$

$$\ddot{\varepsilon}_* \Rightarrow \text{set acceleration.}$$

In the second test the bottom wall is perturbed to the configuration used previously:

$$h(x_3, t) = \varepsilon(t) \sin\left(\frac{2\pi x_3}{L_3}\right). \tag{3.14}$$

After 30 time units (300 steps), wall-normal and spanwise velocities decay to zero and the streamwise solution converges, satisfying the Poisson equation (3.12) to within 10^{-13}. See Table V.

3.2.2. *Dynamic tests.* The tests of subsection 3.2.1 validate the coordinate transformation, but only in a static sense, confirming global convergence to a known steady solution. The decay rate tests of subsection 3.1 confirm the accuracy of the solution locally in time, but the test cases do not depend upon the transformation. Missing is a test of the time accuracy of the time-dependent transformation.

For a direct test of the algorithm, including the explicit time dependence of the boundary conditions, consider flow in a channel with an accelerating wall. As dictated by the solenoidal condition, velocity of the lower wall is matched by an identical velocity of the fluid *through* the upper wall. In the case of a channel with flat walls, the boundary conditions for all Fourier modes but the zeroth are zero, which simplifies the structure of the disturbance: spanwise velocities are zero and streamwise velocity depends only upon x_2. The solenoidal condition then dictates that wall-normal velocity everywhere in the channel be equal to the velocity of the lower wall. Because the second component of velocity is determined trivially through prescription of the boundary conditions, the problem is essentially one-dimensional.

In the computational frame, the evolution equation for mean streamwise velocity is

$$\frac{\partial U_1}{\partial t} = -\left\langle \frac{\partial p}{\partial x_1} \right\rangle - \frac{\dot{\varepsilon}(t)}{2}\left[\frac{1}{2-\varepsilon(t)} + 1 - x_2\right]\frac{\partial U_1}{\partial x_2} + \frac{1}{\mathrm{Re}}\left[\frac{2}{2-\varepsilon(t)}\right]^2 \frac{\partial^2 U_1}{\partial x_2^2}. \tag{3.15}$$

Representing $U_1(x_2, t)$ in Chebyshev space, treating the viscous term implicitly and the convective term explicitly, (3.15) is

$$\left(I - \frac{\Delta t}{\mathrm{Re}}\left[\frac{2}{2-\varepsilon(t^{n+1})}\right]^2 D^2\right)\hat{U}_1^{n+1}(k_2)$$

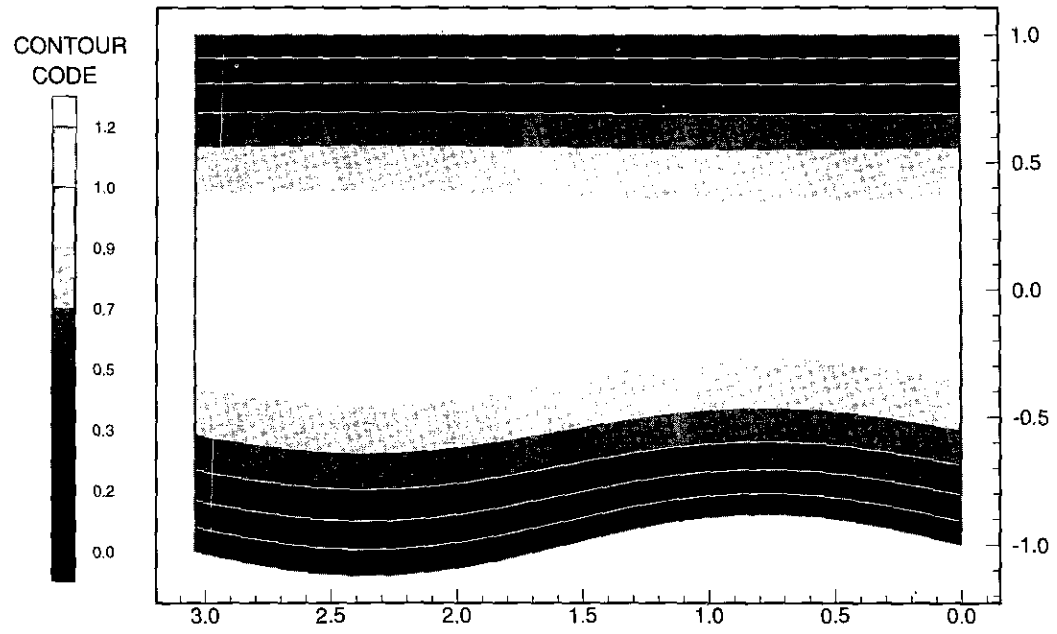

FIG. 5. One-dimensional, steady Stokes flow over a spanwise varying wall (Table V): velocity contours with flow direction out of the page.

$$= \left[I - \frac{\dot{\varepsilon}(t^{n+1})\,\Delta t}{2} \left(\left[\frac{1}{2 - \varepsilon(t^{n+1})} + 1 \right] D - \tilde{D} \right) \right] \hat{U}_1^n(k_2) + \hat{\mathbf{f}}(k_2) \tag{3.16}$$

$$\hat{\mathbf{f}} \equiv \begin{cases} \left\langle \dfrac{\partial \hat{\mathbf{p}}}{\partial x_1} \right\rangle & (k_2 = 0) \\ 0 & (k_2 \neq 0) \end{cases}; \tag{3.17}$$

$\tilde{D}$ is a spectral representation of the convolution operator:

$$x_2 \frac{\partial}{\partial x_2} \to \tilde{D}. \tag{3.18}$$

Boundary conditions are zero and the initial condition is a parabolic profile:

$$\hat{\mathbf{U}}_1(k_2 = 0, t = 0) = 0.5; \quad \hat{\mathbf{U}}_1(k_2 = 1, t = 0) = -0.5. \tag{3.19}$$

The discretization provides only first-order accuracy in time, but the solver is inexpensive, allowing for a small time increment. This solution is advanced in time and the results compared with a flow simulation (using the third-order Runge–Kutta integrator). See Table VI.

During the runs flow perturbations (deviation from the initial parabolic) are of order 10^{-2} and differences in the two solutions never exceed 10^{-4}.

3.3. *The Non-canonical Channel: Higher-Dimensional Flows*

3.3.1. *Stokes flow.* The Stokes approximation (no convection) is valid for low Reynolds number flows across any wall geometries, provided the wall functions are smooth and the wall perturbations not too large. First is a test of flow over a two-dimensional surface which varies sinusoidally in the streamwise direction:

$$h(x_1, t) = \varepsilon(t) \sin\left(\frac{2\pi x_1}{L_1}\right). \tag{3.20}$$

The lower wall is perturbed in time from flat to its final configuration and height. See Table VII. After 30 time units (600 steps), transients due to the velocity of the wall decay to zero and the two-dimensional flow converges to a steady solution (to within round-off error). The salient features of the flow are corroborated by small perturbation theory [26]: streamlines are in phase with the walls (Fig. 6)

TABLE VI

Flow/wall parameters	*Time parameters*	Box *dimensions*	No. of *grid points*
$\mathrm{Re} = 2$	$\Delta t_{\text{1st order}} = 1.0 \times 10^{-5}$	$L_1 = 2\pi$	$N_1 = 16$
$\varepsilon = 0.2[1 - \cos(t)]$	$\Delta t_{\text{3rd order}} = 1.0 \times 10^{-1}$	$L_2 = 2$	$N_2 = 17$
$\dot{\varepsilon} = 0.2[\sin(t)]$	$T = \dfrac{\pi}{2}$	$L_3 = 2\pi$	$N_3 = 16$

TABLE VII

Flow/wall parameters	Time parameters	Box dimensions	No. grid points
$\mathrm{Re} = 2$	$\Delta t \approx 0.05$	$L_1 = \pi$	$N_1 = 32$
$\varepsilon_* = 0.12$	$T \approx 29$	$L_2 = 2$	$N_2 = 33$
$\dot{\varepsilon}_*, \ddot{\varepsilon}_* = 0.01$		$L_3 = \pi$	$N_3 = 16$

Note. See Fig. 6.

TABLE VIII

Flow/wall parameters	Time parameters	Box dimensions	No. grid points
$\mathrm{Re} = 2$	$\Delta t \approx 0.02$	$L_1 = \frac{\pi}{2}$	$N_1 = 40$
$\varepsilon_* = 0.10$	$T = 15$	$L_2 = 2$	$N_2 = 33$
$\dot{\varepsilon}_*, \ddot{\varepsilon}_* = 0.01$		$L_3 = \frac{\pi}{2}$	$N_3 = 40$
$\sigma = 0.19$			

Note. See Figs. 7–9.

Second is a test of flow over a three-dimensional Gaussian protuberance located in the middle of the lower wall ($x_{13}^* = \pi/4$):

$$h(x_1, x_3, t) = \varepsilon(t) e^{-\sigma^{-2}[(x_1 - x_1^*)^2 + (x_3 - x_3^*)^2]}. \tag{3.21}$$

See Table VIII. Even though the channel is shortened to $L_1 = \pi/2$, flow is under-resolved in the streamwise direction (due to the complexity of the wall function). The result is non-zero divergence of order 10^{-7}. Nonetheless, the solution converges to within 10^{-7}, and the flow characteristics match that which is predicted by small perturbation theory. Flow near the lower wall is symmetric about the centerline of the protuberance, streamwise as well as spanwise, corroborating the Stokes approximation (Fig. 7–9). The protuberance creates local pressure maxima on its upstream side which slows the fluid on the approach and accelerates it over the top and around the sides.

3.3.2. *Separated flow.* Last is a simulation of higher Reynolds number flow over a Gaussian protuberance. The Reynolds number (Re = 2083) is high in the sense that it is three orders of magnitude above that used in the tests of Stokes flow; however, it is still below the value which demarks transitional flow. The protuberance is located in the middle of the lower wall ($x_1^* = \pi/2$, $x_3^* = \pi/4$):

$$h(x_1, x_3, t) = \varepsilon(t) e^{-\sigma^{-2}[(x_1 - x_1^*)^2 + (x_3 - x_3^*)^2]}. \tag{3.22}$$

Results of the pseudospectral (PS) simulation are compared with a solution obtained by Mason and Morton [27] using a finite-difference (FD) method. The parameter values used in the PS simulation are listed in Table IX.

Table X provides a comparison of the relevant parameters. The local Reynolds number is based on the height of the obstacle

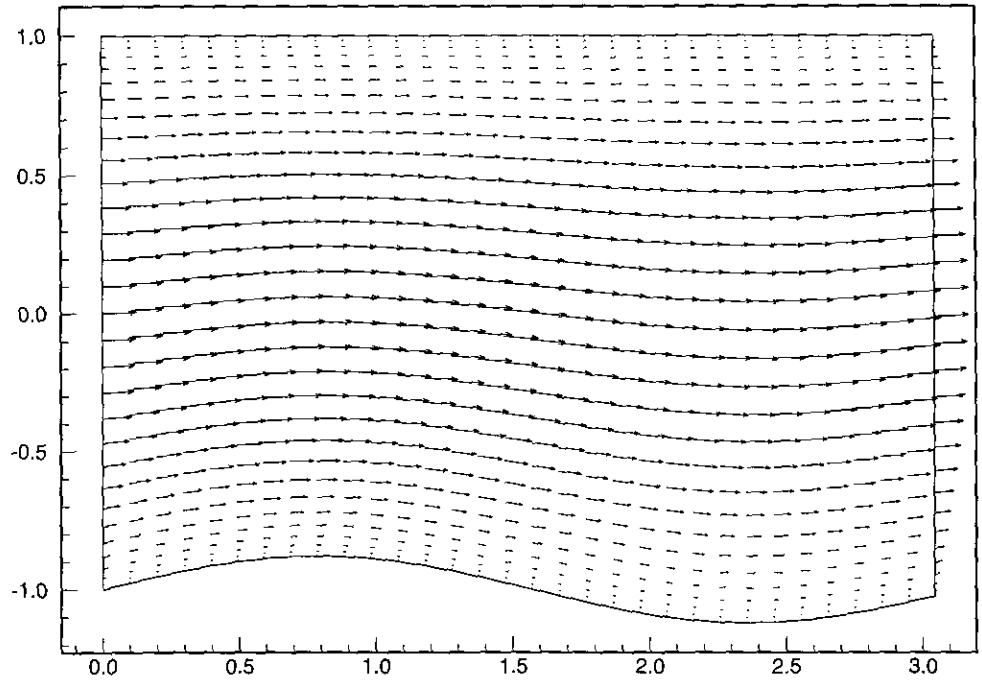

FIG. 6. Two dimensional, steady Stokes flow over a streamwise varying wall (Table VII).

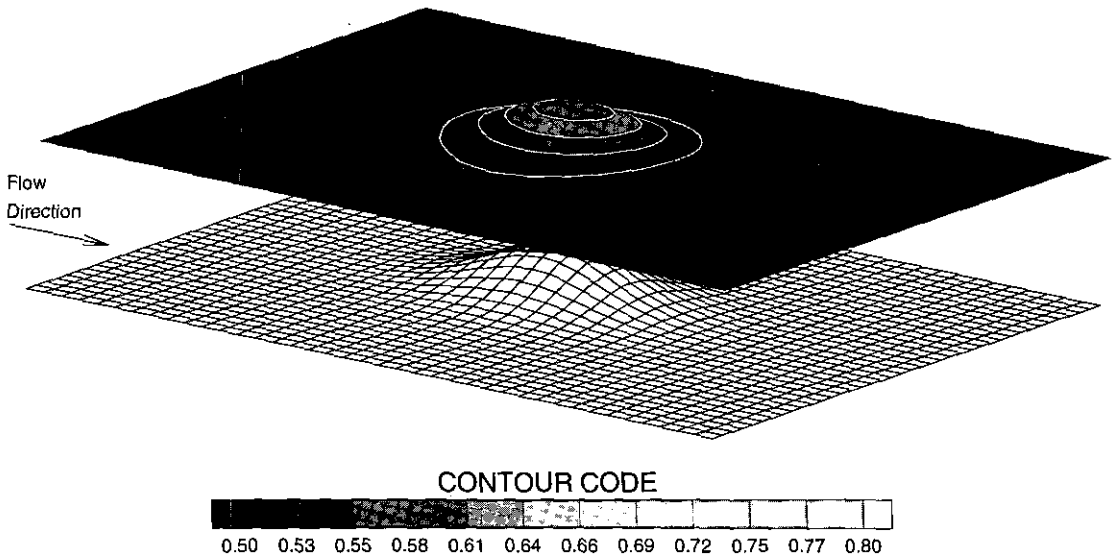

FIG. 7. Three-dimensional, steady Stokes flow over a Gaussian protuberance (Table VIII): streamwise velocity in a plane parallel to and directly above the lower wall.

(ε_*) and the local velocity (the mean velocity that would exist through the height interval in the absence of the obstacle):

$$\mathrm{Re}_l = \frac{U_l \varepsilon_*}{\nu}. \tag{3.23}$$

A constant mass flux is imposed in the PS simulation. The initial field is parabolic and so the local velocity is

$$U_l = \frac{U_0}{\varepsilon_*} \int_{-1}^{\varepsilon_* - 1} (1 - x_2^2)\, dx_2 \approx 0.12 U_0. \tag{3.24}$$

The corresponding boundary layer is uniform in the streamwise direction with the following displacement thickness:

$$\delta = L_0 \int_{-1}^{0} [1 - (1 - x_2^2)]\, dx_2 = \frac{L_0}{3}. \tag{3.25}$$

In the FD simulation a Blasius boundary layer is prescribed and its thickness at the obstacle location is that which is used in the ratio listed in Table X. The FD obstacle shape is defined by

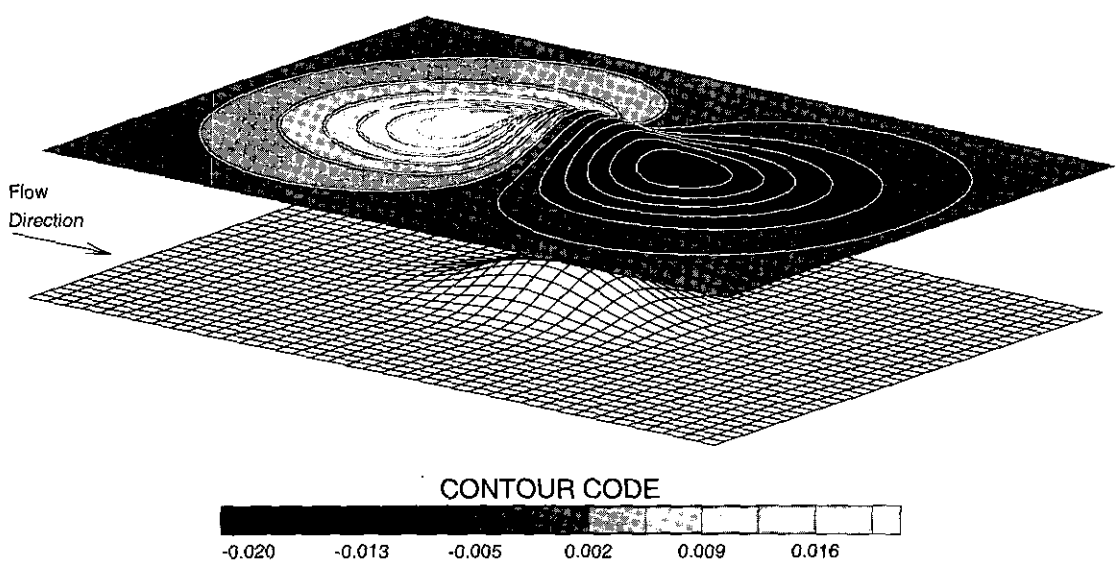

FIG. 8. Three-dimensional, steady Stokes flow over a Gaussian protuberance (Table VIII): wall-normal velocity in a plane parallel to and directly above the lower wall.

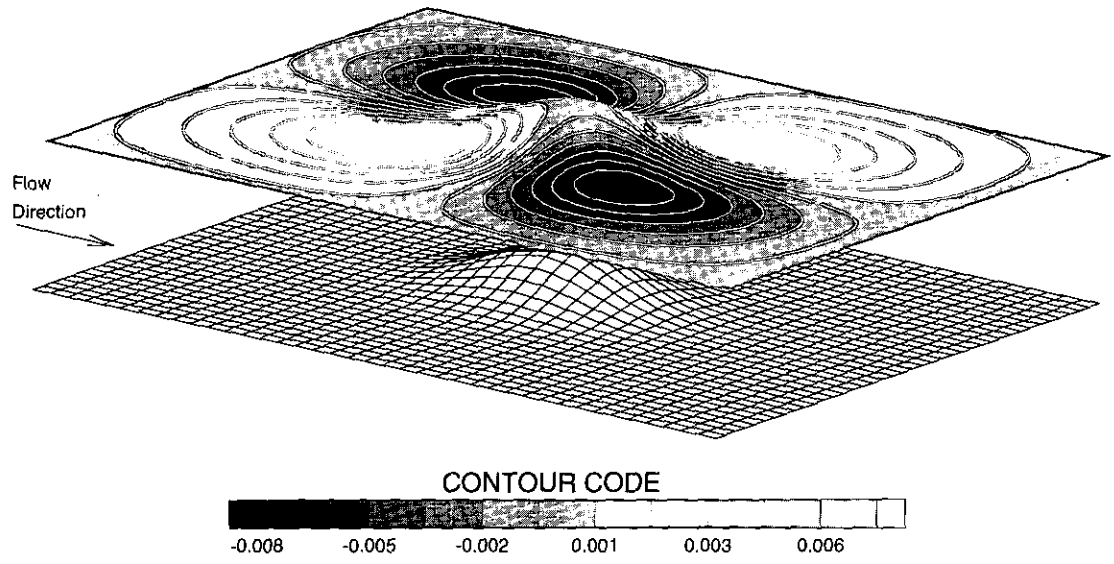

FIG. 9. Three-dimensional, steady Stokes flow over a Gaussian protuberance (Table VIII): spanwise velocity in a plane parallel to and directly above the lower wall.

$$h(x_1, x_3) = \begin{cases} \epsilon \cos^2\left[\frac{\pi}{2}\frac{r(x_1, x_3)}{\sigma}\right] & r(x_1, x_3) < \sigma \\ 0 & r(x_1, x_3) \geq \sigma \end{cases} \quad (3.26)$$

$$r(x_1, x_3) = [(x_1 - x_1^0)^2 + (x_3 - x_3^0)^2]^{1/2}.$$

This shape corresponds closely to the Gaussian. The Gaussian function is chosen because its higher derivatives are continuous and its shape holds up better upon Fourier transformation: the tails remain very close to zero (10^{-8}) as opposed to 10^{-4} in the case of the cosine function of (3.26).

Figures 10 and 11 provide a quantitative comparison of the two solutions. Figure 10 represents the final, steady solution of the PS simulation (at $T \approx 16$), following dissipation of transients associated with the initial upward velocity of the boundary. These contour plots of streamwise vorticity indicate nested pairs of vortices up- and downstream of the obstacle. Closest to the wall are a pair with central upwash (upstream) and a pair with central downwash (downstream). Stacked atop these are weaker pairs of opposite sense. The maxima and minima of streamwise vorticity are located at the wall: ± 0.91 in View A and ± 0.61 in View B. The tip of the protuberance is located at $x_2 = -0.88$, close to the tops of the upper pairs.

From Fig. 11 the shapes of the vortical structures obtained from the FD simulation are almost identical. The maxima/minima at the wall are $\pm 0.4(U_0/\sigma)$ (upstream) and ± 0.29 (U_0/σ) (downstream). Renormalizing with respect to local variables (U_l and ε_*) yields values of $\pm 0.88(U_l/\varepsilon_*)$ upstream and $\pm 0.64(U_l/\varepsilon_*)$ downstream. All values from the PS simulation are normalized by the outer variables. Renormalizing with respect to local variables ($U_l = 0.12U_0$ and $\varepsilon_* = 0.12L_0$) yields maxima/minima of $\pm 0.91(U_l/\varepsilon_*)$ upstream and $\pm 0.61(U_l/\varepsilon_*)$ downstream. The relative differences, then, in the maxima/minima are 3.3% upstream and 4.7% downstream. Considering the substantial (and unavoidable) differences in the prescriptions for mean flow (and in the boundary layer thicknesses), these results are quite close.

Figure 12 contains views of the surface stress pattern at the lower wall (top panel from the FD simulation, third panel down from the PS simulation) and views of the centerplane streamlines (second panel down from FD and bottom panel from PS). The flow direction is from left to right. The surface stress streamlines are constructed from the stream- and spanwise components of the wall shear stress and they indicate flow direction close to the wall. Partial streamlines have been used

TABLE IX

Flow/wall parameters	Time parameters	Box dimensions	No. grid points
$\mathrm{Re} = 2083$	$\Delta t \approx 0.015$	$L_1 = \pi$	$N_1 = 80$
$\varepsilon_* = 0.12$; $\sigma = 0.18$	$T \approx 30$	$L_2 = 2$	$N_2 = 65$
$\dot{\varepsilon}_* = 0.05$; $\ddot{\varepsilon}_* = 0.1$		$L_3 = \frac{\pi}{2}$	$N_3 = 32$

Note. See Figs. 10 and 12–15.

TABLE X

	Re_l	ε_*/σ	U_l/U_0	ε_*/δ
PS	30	0.67	0.12	0.36
FD	30	0.66	0.3	1.2

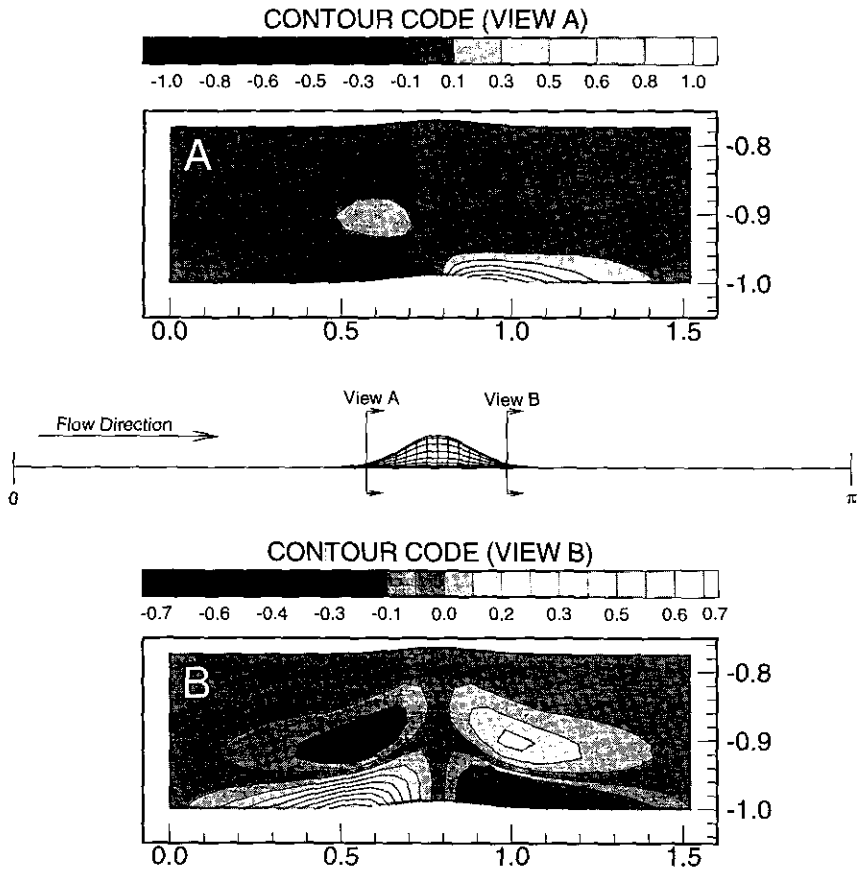

FIG. 10. Steady, separated flow over a Gaussian protuberance (Table IX): streamwise vorticity.

in the third and fourth panels to avoid bunching of the lines in regions of convergent flow. From all four panels, a well-defined zone of separated flow exists downstream of the protuberance, and in general, flow characteristics from the PS simulation match well with those from the FD simulation.

As a final observation, flow over the stationary obstacle generates a normal flux of tangential vorticity at the boundary [26]:

$$\left.\frac{\partial \omega_i}{\partial \mathbf{n}}\right|_{wall} = \varepsilon_{ijk} n_j \left.\frac{\partial p}{\partial \tilde{x}_k}\right|_{wall}; \tag{3.27}$$

$\mathbf{n}$ is a unit vector, normal to the lower wall. The alternating tensor ε_{ijk} is $+1$ when i, j, k are in cyclic order, -1 when i, j, k are in anti-cyclic order, and 0 if any two of the i, j, k are equal. The streamwise pressure gradient drives the flow and contributes most to the production of boundary layer vorticity:

$$\left.\frac{\partial \omega_3}{\partial \mathbf{n}}\right|_{wall} \sim -n_2 \left.\frac{\partial p}{\partial \tilde{x}_1}\right|_{wall}. \tag{3.28}$$

Correspondingly, the steady solution contains a concentration of negative spanwise vorticity at the top of the protuberance (Fig. 13).

4. NUMERICAL STABILITY

As described in subsection 2.5, stability limits associated with time advancement of the convective term are defined by the CFL condition: a fluid particle may travel no more than one computational cell length, width, or height per time step. Additional (independent) stability restrictions do exist, precipitated by the iterative method of solution of the elliptic equations for pressure and velocity. To illustrate consider positive vertical displacement of a flat wall ($\varepsilon > 0$). As in the dynamic test of subsection 3.2.2, the problem is essentially one-dimensional, involving one unknown, mean streamwise velocity, with a prescribed mean streamwise pressure gradient and a prescribed mean wall-normal velocity at the walls (and everywhere else in the channel). The iterative method consists of splitting the viscous operator into an invertible part and the remainder (subsection 2.1).

To determine the stability restrictions associated with this procedure consider only the final steady solution, valid for low Reynolds number flows: the lower wall is displaced from its

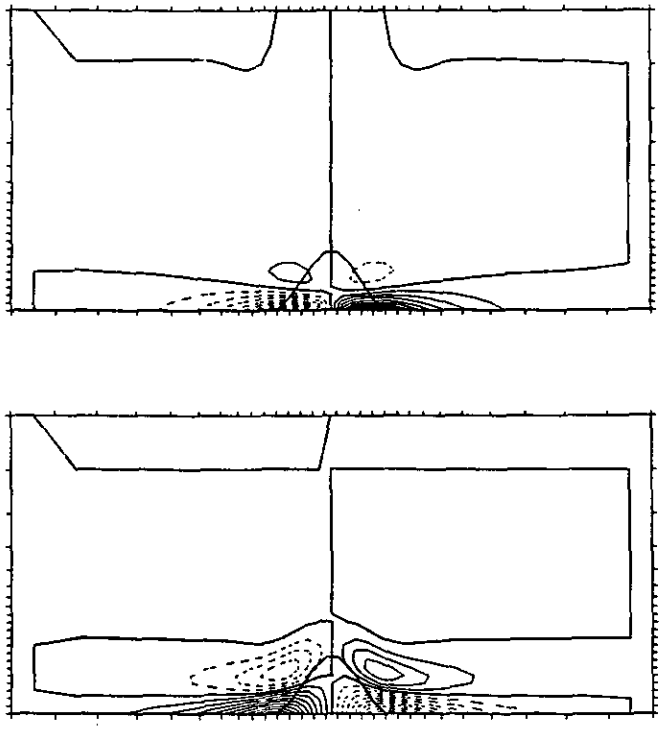

FIG. 11. Steady, separated flow over a 3-D obstacle (from Mason and Morton [27]): streamwise vorticity in transverse sections at the upstream extremity of the obstacle (top panel) and downstream extremity (bottom panel). Solid contours are positive, dashed contours are negative. Contour intervals are 1/10 of the maximum value, and the maxima are 0.4 (U_0/σ) (upstream) and 0.29 (U_0/σ) (downstream). Courtesy of P. J. Mason and B. R. Morton, "Trailing vortices in the wakes of surface-mounted obstacles," *J. of Fluid Mechanics*, (1987).

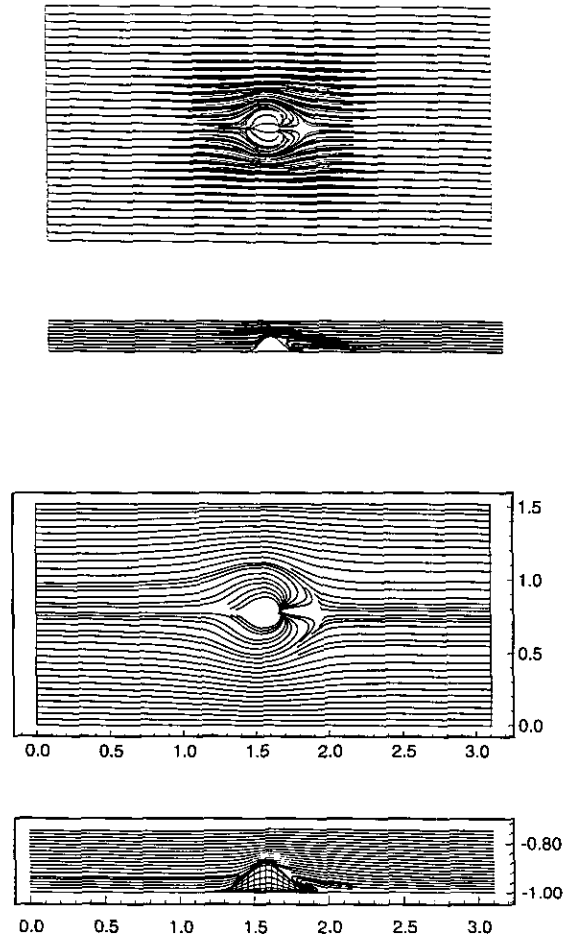

FIG. 12. Separated flow (Tables IX and X): Surface stress pattern at the lower wall (top panel from Mason and Morton [27], third panel down from the pseudospectral simulation) and centerplane streamlines (second panel down from Mason and Morton, bottom panel from the pseudospectral simulation). Courtesy of P. J. Mason and B. R. Morton, "Trailing vortices in the wakes of surface-mounted obstacles," *J. of Fluid Mechanics*, (1987).

initial position but is stationary. Wall-normal velocity is then zero everywhere and the convective term drops out of the Navier–Stokes equation:

$$\left(I - \frac{\Delta t}{\mathrm{Re}} D^2\right) \hat{\mathbf{U}}_1^{s+1}(k_2) = \left(I + \frac{\Delta t}{\mathrm{Re}} \left[\left(\frac{2}{2-\varepsilon}\right)^2 - 1\right] D^2\right) \hat{\mathbf{U}}_1^{s}(k_2) + \hat{\mathbf{f}}(k_2) \tag{4.1}$$

$$\hat{\mathbf{f}} \equiv \begin{cases} \left\langle \dfrac{\partial p}{\partial x_1} \right\rangle & (k_2 = 0) \\ 0 & (k_2 \neq 0) \end{cases}. \tag{4.2}$$

Again, s denotes position in the iteration sequence. The iteration matrix is Q:

$$\hat{\mathbf{U}}_1^{s+1} = Q\hat{\mathbf{U}}_1^{s} + \hat{\mathbf{f}} \tag{4.3}$$

$$Q \equiv \left(I - \frac{\Delta t}{\mathrm{Re}} D^2\right)^{-1} \left(I + \frac{\Delta t}{\mathrm{Re}} \left[\left(\frac{2}{2-\varepsilon}\right)^2 - 1\right] D^2\right). \tag{4.4}$$

The stability limit is defined by the eigenvalues of Q which must be less than unity:

$$\left| \left(I - \frac{\Delta t}{\mathrm{Re}} D^2\right)^{-1} \left(I + \frac{\Delta t}{\mathrm{Re}} \left[\left(\frac{2}{2-\varepsilon}\right)^2 - 1\right] D^2\right) \right| < I; \tag{4.5}$$

$|\ |$ denotes diagonalization. This yields the following requirement:

$$\varepsilon < 2 - \sqrt{2} \quad (\approx 0.58). \tag{4.6}$$

From (4.6) stability depends only upon ε (positive displacement of the lower wall) and the steady solution is space stable [28]: stability is independent of N_2. The limit on ε is confirmed heuristically by perturbing a flat wall in time, using different values of N_2. In all cases the CFL condition ensures stability of the solution as long as $\varepsilon < 0.58$. When $\varepsilon \geq 0.58$ the solution becomes unstable. For the general case in which the wall perturbation is three-dimensional, the solution vector consists of all

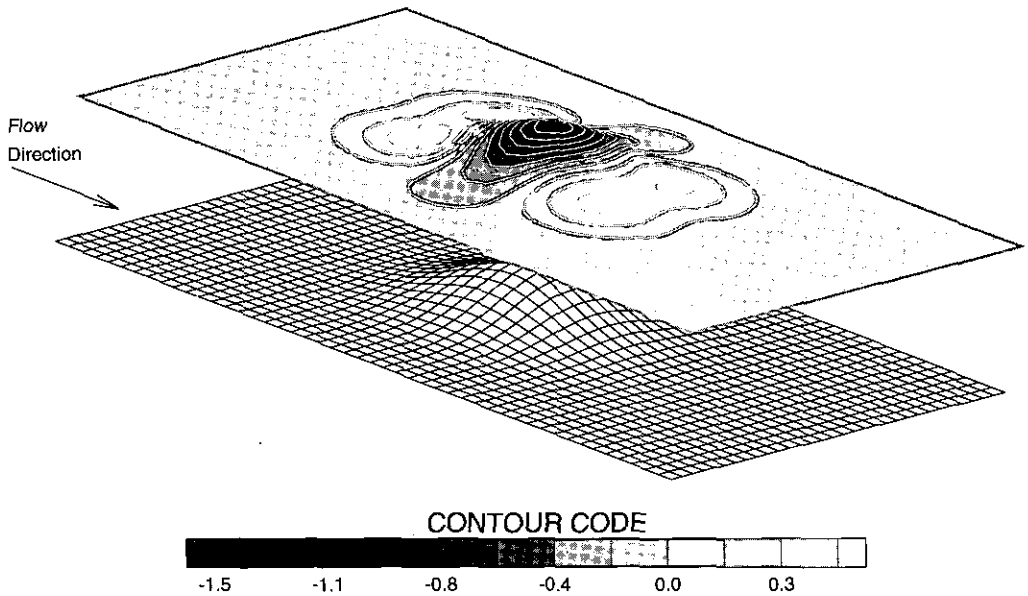

FIG. 13. Three-dimensional, steady, separated flow over a Gaussian protuberance (Table IX): spanwise vorticity in a plane parallel to and directly above the lower wall.

three components of velocity, the pressure, the influence matrix variables, and the tau correction variables:

$$\hat{\mathbf{w}} = \begin{pmatrix} \hat{\mathbf{u}}^1 \\ \hat{\mathbf{v}}_{p,1,2,\tau} \\ \hat{\mathbf{u}}^3 \\ \hat{\mathbf{p}}_{p,1,2,\tau} \\ c_{1,2} \\ \tau_{p,1,2} \end{pmatrix} (k_1, k_2, k_3, t). \tag{4.7}$$

The counterpart of (4.3) is a much larger, more complicated nonlinear system:

$$\hat{\mathbf{w}}^{s+1} = Q\hat{\mathbf{w}}^s + \hat{\mathbf{f}}. \tag{4.8}$$

With a stationary, perturbed wall the elements of the iteration operator Q may depend upon ε, Δt, Re, $L_{1,2,3}$, and $N_{1,2,3}$. Computation of the spectrum of Q is not practicable; however, stability diagnostics may be performed by considering the trivial solution corresponding to quiescent fluid in a channel with a perturbed, stationary wall:

$$\hat{\mathbf{w}}^{s+1} = Q\hat{\mathbf{w}}^s \tag{4.9}$$

$$\hat{\mathbf{w}}^0 = \delta(k_1, k_2, k_3) \quad (\delta \ll 1). \tag{4.10}$$

The iteration operator is the same for the trivial solution of (4.9) as it is for the non-trivial solution of (4.8). Iteration of the actual algorithm is tantamount to iterating on (4.9) and provides an inexpensive way of determining what impact the various parameters have on stability. Additionally, because the trivial solution satisfies the solenoidal condition exactly, components of the solution vector corresponding to the influence matrix ($c_{1,2}$) and the tau correction (τ_p) may be removed to determine what impact these formulations have on the stability restriction.

Using a random number generator to initially fill the solution vector $\hat{\mathbf{w}}$ with values of order 10^{-13} (round-off error), assigning values to the parameters (ε, Δt, Re, $L_{1,2,3}$, $N_{1,2,3}$), and iterating yield rough estimates of the stability limits: stable solutions tend toward machine zero, while unstable solutions grow. First is a test of a stationary, spanwise varying wall. The wall function is defined by (3.11) and the parameter values are listed in Table IV. Keeping the other parameters constant, ε is varied to determine a maximum allowable value. The maximum is approximately 0.12. This limit is also obtained in the case of a non-trivial solution.

Removal of $(c\hat{\mathbf{v}})_{1,2}$ from the solution vector has no impact upon the maximum allowable ε; however, removal of τ_p has a substantial effect. Without the tau correction the stability limit for ε (with all other parameter values as listed on Table IV) increases to well over 0.3. The tau error depends upon the following parameters [20, 21]:

$$\tau_p \propto \frac{\mathrm{Re} \cdot N_2}{\Delta t}. \tag{4.11}$$

From (4.11) the effects of τ_p upon stability should become most pronounced for high Reynolds number flows which re-

TABLE XI

Test No.	Table No.	Converge tolerance	T_{cpu} (h:m:s)	Iterations (max)	Iterations (ave)	Δt (ave)	T	$\eta = T_{cpu}/T$ (min)
1a	V	10^{-13}	1:28:00	14	6.997	0.1013	29.58	2.975
1b	V	10^{-7}	0:28:15	5	3.238	0.1006	18.21	1.551
2a	VII	10^{-13}	2:46:21	13	6.721	0.04899	29.10	5.716
2b	VII	10^{-7}	0:53:24	4	2.959	0.04932	17.85	2.992

quire fine spatial and temporal resolution. To confirm this the test is performed using parameters from Table IX and a Gaussian wall function. The approximate limit for stability is $\varepsilon_{max} = 0.13$. The shape of the wall (curvature) also affects the stability. As an example, halving the standard deviation of the Gaussian protuberance used in the Stokes flow simulation (Table VIII) reduces ε_{max} from 0.17 to 0.10.

5. COMPUTATIONAL EXPENSE

Computations are performed on an IBM 9000-900 and on an IBM SP2 with peak performances of 138 and 266 megaflops and main memories of 1024 megabytes and 2 gigabytes, respectively. The code, fully vectorizable, is run serially (no parallelization). As in all flow simulations, run times are dependent upon the parameters: spatial and temporal resolution, Reynolds number. In the case of the non-canonical channel, run time is also a function of the number of iterations required, which in turn depends upon the resolution, the Reynolds number, the wall perturbation (height, shape, velocity), and the designated accuracy.

Table XI contains, as representative cases, statistics for simulations of Stokes flow across a spanwise varying wall (Tests 1a and 1b) and across a streamwise varying wall (Tests 2a and 2b). The simulations are performed on an IBM SP2 node. As an indication of the impact that designated accuracy has upon computational expense, the tests are executed using two different convergent tolerances, 10^{-13} and 10^{-7}. The simulations were originally performed at the higher tolerances in order to confirm spectral accuracy of the steady solution (subsection 3.2.1). From subsection 2.5 the time accuracy of these low Reynolds number flows is approximately Δt^2 (10^{-3} at best), so that a convergence tolerance of 10^{-7} is certainly reasonable, at least for the transient solutions.

Run times (T_{cpu}) for the streamwise varying wall are approximately double those for the spanwise varying wall because the streamwise resolution is doubled, which (through the CFL condition) halves the time step size. The simulation time (T) corresponds to the lifespan of transients associated with the initial motion of the lower wall: when these transients fall below the convergence tolerance the test is terminated. The maximum wall velocities ($\dot{\varepsilon} = 0.01$) could have been increased by a factor of five without affecting the CFL condition. Accounting for the longer lifespan of the concomitant transients the run times then would be reduced by a factor of three, so that Test 1b, for example, would require approximately 10 minutes of cpu time.

Lowering the convergence tolerance decreases the run time by reducing the number of required iterations and by reducing the required simulation time (T). Lowering the tolerance from 10^{-13} to 10^{-7} reduces run time by a factor of three. More appropriate is a comparison of the ratio of run time (in minutes) to simulation time: $\eta = T_{cpu}/T$. From Table XI the tolerance reduction increases efficiency by a factor of two.

In the simulation of higher Reynolds number, separated flow (Table IX), the specified tolerance is 10^{-7}. As in all of the tests, a maximum number of iterations is required when the wall is still moving and is close to its target height. A representative convergence history is obtained from the simulation of separated flow at $T = 2.032$, as the Gaussian protuberance is rising at its maximum velocity ($\dot{\varepsilon} = 0.05$) and is at 75% of its target height ($\varepsilon = 0.09$). For this test the convergence tolerance was reset to 10^{-12}, requiring 18 iterations.

Figures 14 and 15 are semi-logarithmic plots of the intermediate solution versus position in the iterative sequence (s). Designating the intermediate solution as $\mathbf{u}^s$ and the converged solution as $\mathbf{u}^*$, Fig. 14 is a plot of the maximum value of $|\mathbf{u}^s - \mathbf{u}^*|$ versus s. Figure 15 is a plot of the root mean square (rms) value of this difference, normalized by the rms value of $\mathbf{u}^*$:

$$\left[\frac{\int_0^{L_3}\int_{h-1}^{1}\int_0^{L_1}(\mathbf{u}^s-\mathbf{u}^*)^2\,d\tilde{x}_1\,d\tilde{x}_2\,d\tilde{x}_3}{\int_0^{L_3}\int_{h-1}^{1}\int_0^{L_1}(\mathbf{u}^*)^2\,d\tilde{x}_1 d\tilde{x}_2 d\tilde{x}_3}\right]^{1/2}. \tag{5.1}$$

The solutions ($\mathbf{u}^s$ and $\mathbf{u}^*$) are represented in physical space. The normalized values of Fig. 15 indicate relative error in the intermediate solutions and, in this instance, it is the spanwise component of velocity which leads the field.

As noted in the Introduction, the ultimate purpose of the algorithm is to provide a means of analyzing interactions between a moving boundary and a turbulent boundary layer. At a comparable Reynolds number (Re = 2000), the computational box used in the simulation of separated flow (Table IX) will (given a sufficient perturbation) sustain a turbulent field. The low-order statistics obtained from these minimal flow units

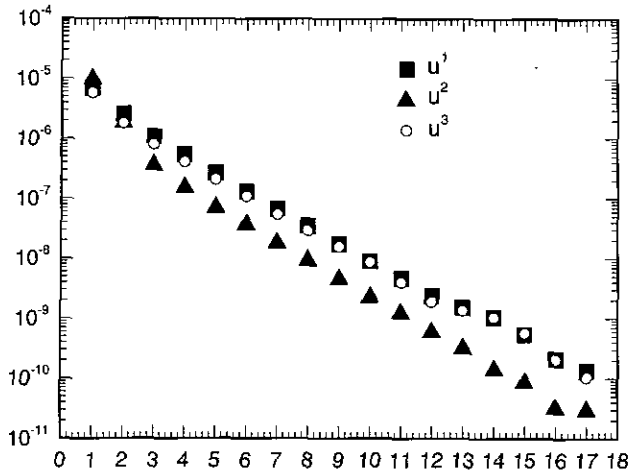

FIG. 14. A convergence history of the separated flow simulation at $T = 2.032$ (Table IX): position in the iterative sequence (s) is plotted on the horizontal axis and the maximum value of $|\mathbf{u}^s - \mathbf{u}^*|$ is plotted on the vertical (where $\mathbf{u}^s$ is the intermediate solution and $\mathbf{u}^*$ the converged solution). The three components of velocity are plotted separately.

match well with experimental data and the simpler wall layer structures provide a clear picture of the associated dynamics [29].

The data of Table XII address the issue of practicality in connection with using a non-canonical, minimal flow unit. In addition to the algorithm associated with a non-canonical channel (NON), one has been written for the canonical channel (CAN). Also a primitive variables, pseudospectral formulation, it has been used to generate a turbulent field in a box of dimensions $L_{1,2,3} = (\pi, 2, \pi/2)$ at a Reynolds number of 2000. Spatial

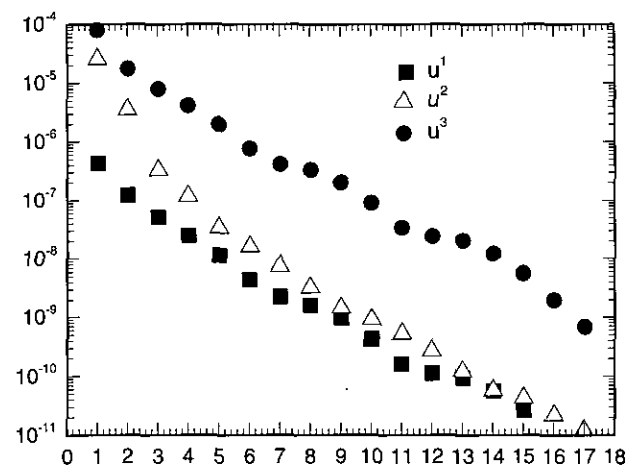

FIG. 15. A convergence history of the separated flow simulation at $T = 2.032$ (Table IX): position in the iterative sequence (s) is plotted on the horizontal axis and the rms value of $|\mathbf{u}^s - \mathbf{u}^*|$, normalized by the rms value of $\mathbf{u}^*$, is plotted on the vertical (where $\mathbf{u}^s$ is the intermediate solution and $\mathbf{u}^*$ the converged solution). Refer to Eq. (5.1). The three components of velocity are plotted separately.

TABLE XII

Test no.	Code	N_1	N_2	N_3	t_{cpu} (min)	%I
1a	CAN	48	65	24	0.10183	
1b	NON	48	65	24	0.25867	61.15
2a	CAN	80	65	32	0.23150	
2b	NON	80	65	32	0.60633	61.76

resolution requirements for the turbulent field are listed in Table XII (Test 1a). Also listed are the resolution requirements for the same box with a Gaussian wall function (Test 2b).

t_{cpu} in Table XII is the cpu time per time step (three substeps), averaged over 100 steps (300 substeps). The runs were performed on an SP2 node. The cpu times listed for Tests 1b and 2b (NON) are measures of expense per step without iteration. %I is the percentage of cpu time consumed during that portion of the algorithm which falls within the iteration loop (Fig. 2). Given i iterations, the total cpu time per step, then, is $[1 + (i - 1)(\%I/100)]\ t_{cpu}$.

Several comparisons are appropriate. From a purely computational standpoint, the NON algorithm is approximately 2.6 times more costly per step, without accounting for iteration expenses, comparing Test 1a and 1b, Test 2a and 2b. Preliminary simulations using the given box with a Gaussian wall function and a turbulent field indicate that an average of four iterations per substep will maintain an accuracy of 10^{-6} ($\sim\Delta t^3$). Using this value, the NON algorithm becomes approximately 7.3 times more costly (again, comparing Test 1a and 1b, Test 2a and 2b).

From a practical standpoint the comparison must be made between Test 1a and Test 2b. Along with the finer spatial resolution comes finer temporal resolution. The ratio of the average time step size of Test 1a to that of Test 2b is approximately $\frac{80}{48}$. Using this ratio and assuming an average of four iterations per substep, the NON algorithm becomes 28 times more costly per unit of simulation time. Conventional analyses of turbulent flows are statistical, requiring simulation times of approximately $T = 200$. This simulation consumes $10\frac{1}{2}$ h of cpu time using the CAN algorithm (Test 1a); using the NON algorithm (Test 2b) will require 300 h.

6. REMARKS

Clearly, a statistical analysis of turbulent flow in a channel with a three-dimensional (e.g., Gaussian) wall function will have to be performed judiciously. One realizable solution to the problem of expense is parallelization: farming out the multiple FFTs and matrix inversions which are executed during each iteration. A full (as opposed to a minimal) flow unit has dimensions of $L_{1,2,3} = (4\pi, 2, 2\pi)$. Kim *et al.* used resolutions of $N_{1,2,3} = (192, 129, 160)$ in their simulation of statistically stationary flow in this full flow unit, requiring approximately 250 CRAY hours per run [5]. In absolute terms then, the addi-

tional expense attached to resolving a three-dimensional wall is offset by beginning with a minimal flow unit.

A major factor with respect to expense, the increase in resolution requirements associated with a non-trivial boundary is a problem intrinsic in any direct method which enforces exact boundary conditions without modeling. In the case of a two-dimensional, spanwise varying wall (riblets), resolution requirements for the wall function are no greater than the requirements for resolution of the turbulence and so expense is increased by a factor of approximately 5.6 (assuming an average of three iterations per substep).

Coupled with the Chebyshev–tau formulation, the iterative method is efficient but does not permit an obvious means of raising those stability limits which are dependent upon ε (Section 4.0). Presumably, changing to a collocation formulation in which a large $(N_1 \times N_2 \times N_3)^2$ matrix is iterated upon would provide this opportunity. Then, for example, a conventional Richardson method would allow for a variable relaxation parameter. However, the impact of the tau correction upon stability is significant, and the remedy for this problem is not so evident. Exact enforcement of the solenoidal condition is itself a requirement for stability. Solving for the primitive variables, even by collocation, requires a tau correction and the problem of stability dependence upon the tau error only assumes a different guise, no less daunting. A velocity–vorticity formulation poses its own, seemingly intractable problems.

Offsetting stability limitations and problems of expense is the unique opportunity that the algorithm provides for the study of transients associated with a variety of flows (laminar, transitional, turbulent) over a variety of surfaces (bumps, dimples, troughs, ridges) which move in time. The lifespans of these transients are an order of magnitude less than the previously mentioned requirements for statistically stationary, turbulent flows. These simulations may be performed affordably with very little preliminary work (compared to the task of devising equivalent experiments in the laboratory), and they provide new access to computational data from direct simulation for a broad class of problems.

ACKNOWLEDGMENTS

The research was supported by Contract F49620-92-J-0287 jointly funded by the U.S. Air Force Office of Scientific Research (Control and Aerospace Programs) and the U.S. Office of Naval Research. G. B. was partially supported by ONR Contract N00014-94-C-0024. Computational resources were provided by the National Science Foundation Supercomputer Facility located at Cornell University. The authors thank A. Pojc of Los Alamos National Laboratory for help in formulating the curvilinear coordinate transformation. Thanks also go to J. Kim, P. Moin, and R. Moser for providing us, at the onset, with their spectral code [5], upon which we cut our teeth and from which we appropriated several very useful ideas.

REFERENCES

1. T. A. Zang, J. P. Drummond, G. Erlebacher, C. Speziale, and M. Y. Hussaini, AIAA Paper, 87-0130, (1987), (unpublished).
2. T. A. Zang and M. Y. Hussaini, AIAA Paper 85-0296, (1985), (unpublished).
3. J. Jimenez, *J. Fluid Mech.* **218,** 265 (1990).
4. R. S. Rogallo and P. Moin, *Ann. Rev. Fluid Mech.* **16,** 99 (1984).
5. J. Kim, P. Moin, and R. Moser, *J. Fluid Mech.* **177,** 133 (1987).
6. J. Jimenez, P. Moin, R. Moser, and L. Keefe, *Phys. Fluids* **31,** 1311–1313 (1988).
7. P. J. Mason and R. I. Sykes, *J. Fluid Mech.* **91,** 433 (1979).
8. M. M. Rai and P. Moin, *J. Comput. Phys.* **96,** 15 (1991).
9. P. W. Duck and O. R. Burggraf, *J. Fluid Mech.* **162,** 1–22 (1986).
10. D. Goldstein, R. Handler, and L. Sirovich, *J. Comput. Phys.* **105,** 354–366 (1993).
11. D. Chu, R. Henderson, and G. E. Karniadakis, *Theoret. Comput. Fluid Dynamics* **3,** 219 (1992).
12. N. Aubry, P. Holmes, J. L. Lumley, and E. Stone, *J. Fluid Mech.* **192,** 115 (1988).
13. G. Berkooz, P. J. Holmes, and J. L. Lumley, *J. Fluid Mech.* **230,** 75 (1991).
14. B. D. Coller, P. Holmes, and J. L. Lumley, Interaction of adjacent bursts in the wall region, *Phys. Fluids* **6,** 954 (1994).
15. P. R. Voke and M. W. Collins, Forms of the generalised Navier–Stokes equations, *J. Engr. Math.* **18,** 219 (1984).
16. T. Gal-Chen and R. C. J. Somerville, *J. Comput. Phys.* **17,** 209 (1975).
17. H. D. Block, *Introduction to Tensor Analysis* (Merrill, Columbus, OH 1978), p. 1.
18. D. Gottlieb and S. A. Orszag, *Numerical Analysis of Spectral Methods* (SIAM, Philadelphia, 1977), p. 143.
19. D. Gottlieb, M. Y. Hussaini, and S. A. Orszag, in *Spectral Methods for Partial Differential Equations*, edited by Voigt *et al.* (SIAM-CBMS, Philadelphia, 1984), p. 1.
20. C. Canuto, M. Y. Hussaini, A. Quarteroni, and T. A. Zang, *Spectral Methods in Fluid Dynamics* (Springer-Verlag, Berlin/New York, 1988).
21. L. Kleiser and U. Schumann, Treatment of incompressibility and boundary conditions in 3-D numerical spectral simulations of plane channel flows, in *Proceedings, 3rd GAMM Conference on Numerical Methods in Fluid Mechanics*, edited by E. H. Hirschel (Vieweg, Braunschweig, 1980), p. 165.
22. P. R. Spalart, R. D. Moser, and M. M. Rogers, *J. Comput. Phys.* **96,** 297 (1991).
23. Guang Yang, Ph.D. Thesis, Cornell University, 31–33 (1992).
24. S. A. Orszag, *J. Fluid Mech.* **50,** 689 (1971).
25. S. A. Orszag and L. C. Kells, *J. Fluid Mech.* **96,** 159 (1980).
26. I. G. Currie, *Fundamental Mechanics of Fluids* (McGraw–Hill, New York, 1974).
27. P. J. Mason and B. R. Morton, *J. Fluid Mech.* **175,** 247 (1987).
28. D. Gottlieb, S. A. Orszag, and E. Turkel, *Math Comput.* **37,** 293 (1981).
29. J. Jimenez and P. Moin, *J. Fluid Mech.* **225,** 231 (1991).
30. H. Schlichting, *Boundary Layer Theory* (McGraw–Hill, New York, 1979).
31. M. J. Lighthill, *Laminar Boundary Layers* (Oxford Univ. Press, Oxford, UK, 1963) p. 48.
32. F. P. Bertolotti, Th. Herbert, and P. R. Spalart, *J. Fluid Mech.* **242,** 441 (1992).
33. C. E. Grosch and S. A. Orszag, *J. Comput. Phys.* **25,** 273 (1977).
34. S. A. Orszag, *J. Comput. Phys.* **37,** 70–92 (1980).
35. S. A. Orszag, A. T. Patera, and R. Balasubramanian, AIAA Paper 83-0229, (1983), (unpublished).